

Article

On the Influence of Scattered Errors over Full-Field Receptances in the Rayleigh Integral Approximation of Sound Radiation from a Vibrating Plate

Alessandro Zanarini 

Dynamics & Vibrations of Machines, DIN—Department of Industrial Engineering, University of Bologna, Viale del Risorgimento 2, 40136 Bologna, Italy; a.zanarini@unibo.it

Abstract: Spatially dense operative deflection shapes and *receptances*, acquired in broad frequency bands, increase the detail in the spatial and frequency domains of the responses of parts in actual dynamic loading, manufacturing and mounting conditions. This work remarks the potential benefits of greater spatial resolution in the Rayleigh integral approximation of sound pressure—here reformulated to exploit the increased quality output from experiment-based optical full-field technologies in contactless structural dynamics—radiated by a vibrating surface in a broad frequency band. But in some cases the noise that is scattered over the estimated *receptance* maps might be heavier, or with different patterns, than expected, with potential repercussions on the sound pressure simulations that come thereof. This work covers this specific latter issue with insight over examples from experiment-based *receptances* of a lightweight vibrating plate. The effects of error spreading are analysed in the space and frequency domains, with special attention to the contribution of the experiment-based full-field *receptance* maps to the accuracy of the vibro-acoustic frequency response function maps.

Keywords: error patterns; sound radiation; vibro-acoustic FRF maps; acoustic transfer functions; Rayleigh integral approximation; optical full-field techniques; experiment-based receptances; full-field FRFs; structural dynamics; NVH



Citation: Zanarini, A. On the Influence of Scattered Errors over Full-Field Receptances in the Rayleigh Integral Approximation of Sound Radiation from a Vibrating Plate. *Acoustics* **2023**, *5*, 948–986. <https://doi.org/10.3390/acoustics5040055>

Academic Editors: Yat Sze Choy and Jian Kang

Received: 16 January 2023
Revised: 8 August 2023
Accepted: 21 August 2023
Published: 24 October 2023



Copyright: © 2023 by the author. Licensee MDPI, Basel, Switzerland. This article is an open access article distributed under the terms and conditions of the Creative Commons Attribution (CC BY) license (<https://creativecommons.org/licenses/by/4.0/>).

1. Introduction

Sound radiation simulations from vibrating surfaces can be achieved by means of linear structural finite element, boundary element or analytical models [1–8], sometimes overly simplified on the real and effective boundary conditions, frictions, mistuning and non-linearities from actual parts and mounting pre-loads, but also without real-life errors. The shape of the error patterns on structural vibrations might be therefore unknown, or disregarded as minor issues as in [9], but the question of whether these errors might be a concern for vibro-acoustic simulations may arise, independently from the specific algorithm used. In the presentation of the work [10], it was underlined how the error in the vibration measurement does not affect the simulations of the acoustic field, since the effects on the Rayleigh integral approximation cancel them out as the error should be uniformly distributed. By using the same approximation, this statement asked for an extended check, based instead on real, more accurate, higher spatial resolution and broad frequency band full-field optical measurements, as can be found in the present extended discussion, working on the *receptances* obtained in [11–14], where, instead, the measurement noises were found with different patterns than the simplistic uniform distributions.

Furthermore, most of the times, the vibro-acoustic investigations may be limited to a single active structural eigenmode at its eigenfrequency, taken alone as a distributed vibrating source in a single tonal or resonance propagation, disregarding the neglected adjacent structural dynamics' contributions. Spatially detailed operative deflection shapes and *receptances*, coming from broad frequency band real testing as in [14,15], instead, may be a viable dataset for the best achievable representation in the spatial and frequency domains

of the real behaviour of manufactured and mounted components around their working load levels, without any simplifications, usable also with a modally dense and damped structural dynamics and complex patterns in the dynamic signature of the excitations, with broad frequency spectra.

At the core of this paper, therefore, the exploitation of experiment-based optical full-field technologies is proposed for sound radiation numerical simulations. A trace of the author's background needs to be given to the interested reader, to understand how the experience with full-field techniques has grown before the recent works [16–22], which are spin-off activities after the end of the TEFMA project (*Towards Experimental Full Field Modal Analysis*, funded by the European Commission with the Marie Curie FP7-PEOPLE-IEF-2011 PIEF-GA-2011-298543 grant and carried out by the author from 1 February 2013 to 31 July 2015 at the Vienna University of Technology, Austria; note: A. Zanmarini was the unique scientific proposer and experienced researcher in the TEFMA project). The early steps were made in the HPMI-CT-1999-00029 *Speckle Interferometry for Industrial Needs* Post-doctoral Marie Curie Industry Host Fellowship project held by the author in 2004–2005 at Dantec Ettemeyer GmbH, Germany. Since the early measurements [23,24] it became clear how the ESPI approach, a *native* full-field optical technology, allows a dense mapping of the structural dynamics for enhanced assessments [25] and fatigue spectral methods [26,27]. The TEFMA project's ideas were born in the works of [25], with the first presentations in [11,28], followed by [12,29–31]. In [13] a gathering of the works of TEFMA was firstly attempted, whereas [14] made an extensive description of the whole *receptance* testing and [32] detailed the successful EFFMA and the full-field based model updating attempts. Only in [33] the full-field techniques were scrutinised to find the potential error distributions on the shapes at each frequency line: this analysis underlined the specific noise patterns in full-field dynamic testing later here used for the results and the discussion. Furthermore, the precise comparison in [34], about new achievements for *rotational* and *strain FRF* high resolution experiment-based *maps*, put again into evidence the quality of full-field datasets, as the numerical derivatives can easily spread errors across the spatial domain. The interested reader can appreciate in [13,29,34] the effect of the measurement noise on derivative quantities; however, unfortunately due to the complexity of their measurement, the *rotational dofs* are usually disregarded, whilst they are relevant for the successful build of a reliable dynamic model for complex structures [35–42]. Based on the achievable *strain FRF* mapping, in [17] a risk index was introduced as a metric to distinguish failure-exposed areas in a dynamically loaded component, with a focus also on the evidences from a damaged fibreglass reinforced composite panel [16,24]. In [19] a comparison among risk index maps was made, when the same white noise spectrum was changed in injection locations, whereas in [20] the variability of risk maps was analysed by the changes in the excitation dynamic signature. In [21] two excitation signatures and two energy injection locations were combined for risk grading. Therefore, various works have been published recently by the author on the full-field optical measurements and on their perspectives in NVH [11–14,16–22,28–32,34]. Especially the latest works [11,13,14,16–22,29,32,34] from the TEFMA project highlighted the tangible advances for the consistency and continuity of the data fields, which have become available by the growing full-field techniques, with clear effects in model updating, derivatives' calculations (*rotational dofs*, *strains*, *stresses* and *risk index maps*) and vibro-acoustics. Optical full-field *receptance* maps are becoming an increasingly consistent non-contacting experiment-based means in the estimation of high spatial resolution dynamic deflection shapes, and are appreciated especially in the case of lightweight structures or panels. These experiment-based shapes come with low, but not null, noise on the fields, across a broad frequency range, with all the blending, and potential phase delays, of a modally dense dynamics, without the need of any analytical model nor of a truncated modal base identification [36,39].

To be recalled is that full-field optical measurements started as a qualitative design aid, thanks to the larger and denser vision offered and the high consistency of the viewed field [43]; but, as based on the chemical development of film compounds, they were not

competitive in terms of time-to-result [44] with the digital instruments of the time. But they were proficiently used to show the whole response shape of a structure at a particular frequency of interest, as they already offered a highly detailed picture of the spatial domain against the coarse representation obtained by traditional lumped sensors (e.g., accelerometers or strain gauges, at that time, the only quantitative instruments). Indeed full-field optical approaches were among the first techniques that showed the entire field ODSs with rapidly changing patterns during the frequency sweeps. These ODSs appeared for the first time as functions of the complex blending of the structural dynamics in non-conventional patterns, highlighting where the best location for the lumped vibration sensors, used in contemporary structural dynamics' approaches, could have been.

SLDV [39] introduced the concept of contactless measurement—adding no mass to the specimen—in time/frequency domains in the 1980s, expanding it to finer grids of scanned locations, thus extending the concept of the velocity sensors to a spatially detailed acquisition. Therefore SLDV is considered *the reference* in NVH when spatially detailed FRF measurements are needed: SLDV keeps the same peculiarities of lumped sensor technologies (and of established procedures, born to exploit few dofs only), but adds many dofs in the spatial domain at a reasonable cost, with a trade-off at high frequency in the sensitivity between displacements and accelerations. Due to the *asynchronous* scanning process, however, SLDV can not be properly called a *native* full-field instrumentation.

Only the optical full-field technologies that acquire the motion-related information from photons *synchronously* recorded at every sensible site of an imaging sensor, normally in a much denser grid, can be instead called *native*. Earlier, in [23,24], the author proved the high quality of the datasets obtainable in the spatial domain from the native full-field measurement techniques, acknowledged in terms of consistency of the motion field among the neighbouring dofs. Since the 2000s, ESPI, among the *native* full-field technologies, has given extremely accurate displacement fields up to several kHz of frequency. Due to a lack of complete processing automation, up to now the main drawback of ESPI remains the time-consuming stepped sine excitation/acquisition, in order to have data at all the lines of a broad frequency band in stroboscopic light acquisitions [25,45].

High-speed DIC is another *native* technology, with its first commercial prototypes starting around 2005. DIC can have good detail in the time-resolved displacement maps, but the processing of the correlated data can be time consuming [12,13]. Due to both a sensor/electronics bandwidth trade-off, between resolution and sampling rate, and the difficulty in properly exciting the higher frequency displacement components, DIC is generally more limited for complex structural dynamics in a broad frequency domain, although rapid electronics and processing improvements can be easily foreseen in the near future. Indeed, nowadays, *scanning* and *native* full-field optical technologies allow displacement and velocity measurements in a non-contact way with dense spatial mapping, without inertia-related distortions of the dynamics (due to added sensors, fixtures and cabling), and without any structural finite element (FE) or analytical models to be accurately tuned for the lumped sensor data expansion [42,46,47]. As it was previously shown in [13,34], ESPI technology actually permits the most precise estimation from non-contacting testing of superficial *receptance* FRF maps, which turn out to be optimal also for derived quantities like dense mapping of *rotational dofs* and *strains*.

The Rayleigh integral formulation (e.g., in [1,4–6,8,48–51]) can be adopted for the numerical approximation of the Helmholtz equation for the sound pressure field induced by a vibrating surface. The Rayleigh approach has undergone a slight re-formulation to take advantage of the spatial oversampling of full-field *receptances* [36,39], here from a lightweight rectangular plate in a broad frequency band. The re-formulation shows how the most advanced experiment-based knowledge available can augment the fidelity of the acoustic field mapping. The results are well detailed maps of the vibro-acoustic frequency response functions (pressure over force), or of the radiated acoustic pressure, once the structural excitation is defined in its dynamic signature and energy injection location. This underlines the importance of the test-based *complex-valued* structural dynamics in

reliable sound radiation predictions. The usage of experiment-based optical full-field *receptances* for the acoustic field prediction has already been introduced by the author in the works [18,22], with interest on the excitation dynamic signature and on the energy injection location. Therefore the accuracy in the maps of experiment-based optical full-field *receptances* becomes crucial for assessing error effects, by means of the here-proposed experiment-based approximation of sound radiation from a vibrating plate, thanks to the high quality estimations of the real structural dynamics with accurate spatial description for complex pattern sensing, especially for lightweight structures in broad frequency bands.

A thin and lightweight rectangular plate was the sample used here, whose dynamics was sensed using the SLDV technology, in a broad frequency band, during the fundamental research project TEFMA. The TEFMA project made a comparison between the state-of-the-art technologies in image-based (*native*, DIC and ESPI) full-field optical measurements and the *scanning* SLDV as reference, to understand if these approaches, not completely established, can provide NVH applications with enhanced peculiarities. A dual-shaker-driven broad frequency band excitation was used successfully for a complete EFFMA as in [32]. The *experiment-based full-field FRF* approach in [14] can bring the complete and real structural dynamics into sound radiation approximations, therefore, as proposed here, assessing the effect of errors, spread on the experiment-based full-field *receptances*, onto the vibro-acoustic simulations. From the perspective of using only experiment-based quantities—for the retained dynamics, for the broad frequency spectra of the excitation and for the high resolution mapping achievable—the quality of the raw dataset plays an uttermost relevance in the accurate and reliable acoustic field reconstruction.

The novel strength of this paper deals with the findings of experiment-based specific noise patterns on the *raw receptances* of the testing, specifically as a uniformly distributed and amplitude-modulated noise, a measurement-related noise and a filtering-related noise. This approach is different from discussing the methods for the best reconstruction of the acoustic fields, as can be found in [52]. Here the errors are in the full-field *raw receptances* only, while the Rayleigh integral is kept as the unique computational means to see the impact on the vibro-acoustic FRFs. The use of a *complex-valued* re-formulation of the Rayleigh integral approximation permits the usage of real measurements without any assumptions, except those concerning the linearity of the system during the *receptances'* estimations [36,39,53]. The assessed noise patterns from real testing, being different from the generally assumed uniform distribution of random noise, have therefore been extensively discussed here, by means of quantitative comparative tools, regarding their potential to create distortions on the simulated vibro-acoustic frequency response function maps, at different distances from the vibrating plate.

This paper is organised as follows. After this introductory Section 1, the main methodological Section 2 comprises what is needed to understand and replicate the analyses of this work: the experiment-based FRF modelling is sketched in Section 2.1; the testing is briefly outlined in Section 2.2, with attention on the set-up; the Rayleigh integral re-formulation is recalled in Section 2.3; the tools to quantitatively compare the simulations are gathered in Section 2.4. The main results' Section 3 proposes the simulations of the vibro-acoustic frequency response functions and the potential error effects, with detailed figures and comments. Section 3.1 deals, after notes on the meshing of the acoustic domain, with examples in the space and frequency domains of vibro-acoustic transfer functions, simulated from the *experiment-based full-field receptance maps*, with and without noise; furthermore, the comparative tools are applied to these simulations. Section 3.2 discusses the effects of a uniformly distributed and amplitude-modulated noise. Section 3.3 discusses the effects of a measurement-related noise. Section 3.4 discusses the effects of a filtering-related noise. The main discussion is done in Section 4, which synthesises the comments of the achieved results, before Section 5 for the final statements. "Abbreviations" finally gathers the nomenclature used in the manuscript without explicit explanation.

2. Materials and Methods

This section contains the tools that were used to make the in-depth analysis of the experimental structural dynamics' errors that can be projected onto the vibro-acoustic FRF simulations. Therefore, the description of the experimental modelling of the structural vibrations is given in Section 2.1; Section 2.2 follows a lumped picture of the experimental activities and testing done in the laboratory; a reformulation of the Rayleigh integral is suggested in Section 2.3 to be able to exploit the *experimental receptances*; finally some tools for the quantitative comparisons are introduced in Section 2.4.

2.1. Direct Experimental Modelling for Full-Field FRFs

The impedance-based studies by means of full-field optical measurements were the pivot of all the activities in the TEFFMA project. The latter were thoroughly investigated to achieve highly reliable full-field FRFs with unprecedented spatial resolutions, for any further speculation that may come, either from testing or from numerical models, also in hybrid frameworks, like those of transfer path analysis (TPA) [41,54,55].

The well known formulation of the *receptance* matrix $\mathbf{H}_d(\omega)$, as a spectral relation between displacements and forces under the assumption of noise only in the output (H_1 estimator [36,39,53]), will be used for the full-field FRFs estimation. $\mathbf{H}_d(\omega)$ describes the dynamic behaviour of a testing system, with potentially multi-input excitation (here 2 distinct shakers) and *many*-output responses (here also several thousands covering the whole sensed surface), as can be formulated in the following *complex-valued* equation:

$$H_{d_{ij}}(\omega) = \frac{\sum_{k=1}^N S_{X_i F_j}^k(\omega)}{\sum_{k=1}^N S_{F_j F_j}^k(\omega)} \in \mathbb{C}, \quad (1)$$

where X_i is the output displacement at i -th dof induced by the input force F_j at j -th dof, while $S_{X_i F_j}^k(\omega)$ is the k -th *cross power spectral density* between input and output, $S_{F_j F_j}^k(\omega)$ is the k -th *auto power spectral density* of the input and ω is the frequency, evaluated in N repetitions.

If the *smoothed receptance matrix* $\hat{\mathbf{H}}_{d_j}(\omega)$ can be evaluated from the *raw receptance matrix* $\mathbf{H}_{d_j}(\omega)$, directly estimated in test sessions from Equation (1), as

$$\hat{\mathbf{H}}_{d_j}(\omega) \approx \lim_{\text{errors} \rightarrow 0} \mathbf{H}_{d_j}(\omega) \in \mathbb{C}, \quad (2)$$

a *receptance error function* $\mathbf{e}_{\mathbf{H}_{d_j}}(\omega)$ can be defined as:

$$\mathbf{e}_{\mathbf{H}_{d_j}}(\omega) = \mathbf{H}_{d_j}(\omega) - \hat{\mathbf{H}}_{d_j}(\omega) \in \mathbb{C}. \quad (3)$$

Once the specific *excitation signature* $F_j(\omega)$ is known in the frequency domain, the FRF formulation in Equation (1) can be used to obtain the full-field displacements over the entire surface, as follows at the specific output dof i :

$$d_{ij}(\omega) = H_{d_{ij}}(\omega)F_j(\omega) \in \mathbb{C}, \quad (4)$$

or for the whole *displacement vector* \mathbf{d}_j due to the excitation in dof j as:

$$\mathbf{d}_j(\omega) = \mathbf{H}_{d_j}(\omega)F_j(\omega) \in \mathbb{C}. \quad (5)$$

The surface *velocity vector* \mathbf{v}_j due to the excitation in dof j easily comes as:

$$\mathbf{v}_j(\omega) = -i\omega\mathbf{d}_j(\omega) = -i\omega\mathbf{H}_{d_j}(\omega)F_j(\omega) \in \mathbb{C}. \quad (6)$$

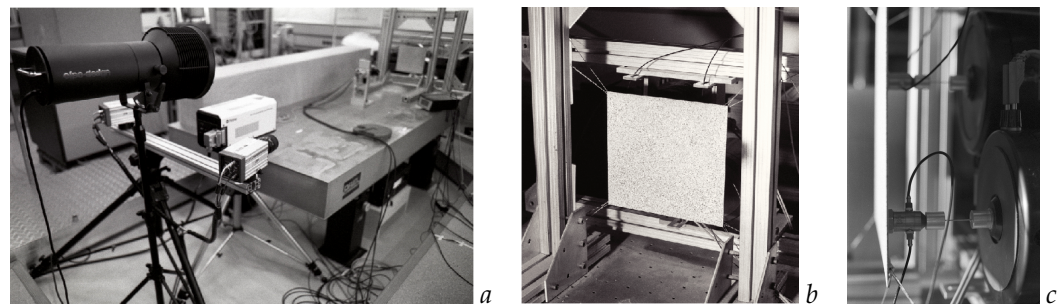


Figure 1. Full-field optical measurement instruments set-up in front of the specimen on the anti-vibration table with shakers on the backside: the instruments in (a), the restrained thin plate in (b) and the 2 shakers in (c).

Analogously to Equation (3), a *displacement error function* $e_{d_j}(\omega)$ and a *velocity error function* $e_{v_j}(\omega)$ can be defined when using the *smoothed receptance matrix* $\hat{\mathbf{H}}_{d_j}(\omega)$ in a *smoothed displacement vector* $\hat{\mathbf{d}}_j(\omega) = \hat{\mathbf{H}}_{d_j}(\omega)F_j(\omega)$ and *smoothed velocity vector* $\hat{\mathbf{v}}_j(\omega) = -i\omega\hat{\mathbf{H}}_{d_j}(\omega)F_j(\omega)$, as:

$$e_{d_j}(\omega) = \mathbf{d}_j(\omega) - \hat{\mathbf{d}}_j(\omega) \in \mathbb{C}, \quad (7)$$

$$e_{v_j}(\omega) = \mathbf{v}_j(\omega) - \hat{\mathbf{v}}_j(\omega) \in \mathbb{C}. \quad (8)$$

Increasing the spatial resolution in dynamic models by means of *many* dofs full-field FRFs will be therefore a valuable addition to the state-of-the-art of the design of complex systems; it will surely lead to the exploration of new FRF-based quantities derived from excellent quality displacement fields, such as surface rotations, velocities, strains & stresses and failure point distributions [13,19–21,29–32,34]. Furthermore, distributed loading patterns, such as those resulting from vibro-acoustics [18,22], can be considered.

2.2. The Lab Activities for the TEFFMA Project in Brief

In the well equipped laboratory of the TU-Wien it was possible to organise a complex set-up for the comparison of the three different technologies available there for acquiring full-field FRFs: SLDV, high-speed DIC and dynamic ESPI. The interested reader can find more details about TEFFMA in [14], while for the physics' principles of each instrumentation see instead [43,44,56–58]. As can be seen in Figure 1a, the lab had a dedicated underground room with seismic floor and air-cushioned anti-vibration optical table, to filter out the environmental vibrations. The specimen in Figure 1b was placed at around 1.5 m from the closest wall to avoid significant sound reflections, also limited by the shape of the shakers in Figure 1c and of the discontinuities of the equipment behind, as in Figure 1a. Table 1 confirms the decreasing influence of potentially wall-reflected sound waves, especially as the frequency and distance increase. Therefore the vibrating plate can be considered a good approximation of the infinite baffled surface required in Rayleigh approach [1,7], later used, where only the plate is in limited out-of-plane motion, the air around being still. A Polytec PSV 300 was at disposal as a scanning LDV reference system, with the 1D (out-of-plane) scanning head OFV-056. The image-based full-field gears consisted of: the Dantec Ettmeyer Q-500 Hi-Res, as an ESPI system for 3D dynamic measurements in stroboscopic coherent laser light; and the Dantecdynamics Q-450, for 3D dynamic DIC acquisitions by means of high-speed cameras in high-frequency and -power white light. Great attention was paid to understand the limits and requirements of all these technologies in order to achieve a common framework for the measurements, around the same linearisation of the structural dynamics. A promising compromise was achieved in the range [20–1024] Hz, with the 3 techniques having their own spatial and frequency resolutions.

Table 1. Amplitude samplings of Green's function with distance and frequency dependencies, $c_0 = 300$ m/s.

Distance	20 Hz	250 Hz	512 Hz	750 Hz	1024 Hz
1 mm	7.954e+01	7.916e+01	7.873e+01	7.834e+01	7.789e+01
2.5 mm	3.180e+01	3.142e+01	3.099e+01	3.061e+01	3.017e+01
5 mm	1.588e+01	1.550e+01	1.508e+01	1.471e+01	1.430e+01
15 mm	5.272e+00	4.904e+00	4.517e+00	4.192e+00	3.846e+00
25 mm	3.150e+00	2.793e+00	2.435e+00	2.149e+00	1.862e+00
50 mm	1.559e+00	1.225e+00	9.310e-01	7.256e-01	5.446e-01
75 mm	1.028e+00	7.164e-01	4.747e-01	3.267e-01	2.124e-01
150 mm	4.982e-01	2.419e-01	1.062e-01	5.028e-02	2.126e-02
200 mm	3.659e-01	1.396e-01	4.660e-02	1.719e-02	5.457e-03
300 mm	2.339e-01	5.514e-02	1.063e-02	2.383e-03	4.260e-04
500 mm	1.291e-01	1.161e-02	7.469e-04	6.178e-05	3.505e-06
750 mm	7.750e-02	2.091e-03	3.411e-05	8.116e-07	1.097e-08
1 m	5.234e-02	4.235e-04	1.753e-06	1.199e-08	3.861e-11
1.5 m	2.830e-02	2.059e-05	5.484e-09	3.104e-12	5.669e-16
2 m	1.722e-02	1.127e-06	1.930e-11	9.036e-16	9.364e-21
3 m	7.550e-03	3.997e-09	2.834e-16	9.079e-23	3.029e-30

The experimental set-up was designed in order to let all the three measurement technologies focus on the same dynamic behaviour, thought to have a high modal density inside the frequency range of interest. A thin aluminum rectangular plate (external dimensions in mm: $250 \times 236 \times 1.5$) was fixed by wires to a rigid frame on the air-spring optical table (see Figure 1b) to restrain any excessive rigid-body movement. The plate was in pristine condition, so as not to confuse the measurement errors with part's defects [16,24]. The front side of the plate was sprayed with a DIC-friendly random noise pattern paint layer. The excitation was given by two electrodynamic shakers positioned on the back side of the plate, to fulfil the stepped-sine phase-shifting acquisition procedure for ESPI with an external sine waveform generator, while the LMS Test.Lab system drove the shakers' excitations in SLDV and DIC measurements. The force signals were sampled at the shaker-plate interfaces by means of the force cells in the impedance heads, to calculate the *receptance* FRFs as in Equation (1).

ESPI permitted the assessment, fixing and thus prevention of unwanted vibrations from any part of the rig up to much higher frequencies than those in the common overlapping: this means that the output motion of the specimen was highly coherent with the input force [11,13,14], for the best achievable measurements. Great attention was also paid to the optical alignments of all the instruments; the depth of field of each optics was accurately selected to match the structural dynamics' requirements, in terms of collected photons and dynamic range for the best image quality, thanks to the extended practice of photography of the author (see fine art, nature and wildlife photography at https://www.colorazeta.it/index_EN.htm, accessed on 23 April 2023). The gained experience with full-field optical measurements revealed itself, together with that of photography, as pivotal in arranging the multiple camera acquisition for photogrammetry [58] tests in [59,60]. Interested readers can widen their understanding in [13,14,34], to appreciate the spatial consistency and continuity of the data, with clean shapes, sharp nodal lines and excellent *Coherence functions* [36,39,53], especially from ESPI. SLDV was used here, though, as the most established and widespread source available of non-contacting experimental data for the specific purpose of evaluating the *raw receptances'* error impacts on *vibro-acoustic FRF maps*.

2.3. Revisiting the Sound Pressure Radiation Formulation

The vibro-acoustic simulation here discussed concerns the sound radiated to an infinite acoustic domain by a finite vibrating surface mounted on an infinite baffle to avoid any other uncontrolled source or reflection, i.e., the plate whose structural dynamics was here measured, as explained in Section 2.2. The case is that of propagating waves [61] in an infinite medium, with a frequency domain approach: in the a -th point of global coordinates \mathbf{a}_a of the acoustic domain A , the sound pressure $p(\mathbf{a}_a, \omega)$ can be defined, according to [1,4,6,8,49–51], from the Helmholtz equation as:

$$p(\mathbf{a}_a, \omega) = \frac{i\omega\rho_0}{2\pi} \int_S v_n(\mathbf{q}_q, \omega) \frac{e^{-ikr_{aq}}}{r_{aq}} dS \tag{9}$$

or

$$p(\mathbf{a}_a, \omega) = 2i\omega\rho_0 \int_S v_n(\mathbf{q}_q, \omega) G(r_{aq}, \omega) dS, G(r_{aq}, \omega) = \frac{e^{-ikr_{aq}}}{4\pi r_{aq}} = \frac{e^{-i\omega r_{aq}/c_0}}{4\pi r_{aq}}, \tag{10}$$

where i is the imaginary unit, ω is the angular frequency ($\omega = 2\pi h$, with h being the time frequency in Hertz), ρ_0 is the medium (here just air) density, $v_n(\mathbf{q}_q, \omega)$ is the normal (out-of-plane) velocity of the infinitesimal vibrating surface dS located in the global coordinate \mathbf{q}_q , \mathbf{q} representing the whole vector of coordinates of the vibrating surface S , $k = \omega/c_0 = 2\pi/\lambda$ is the wavenumber in the Helmholtz equation, c_0 is the speed of sound at rest in the medium, λ is the acoustic wavelength, $r_{aq} = \|\mathbf{r}_{aq}\|$ is the norm of the distance $\mathbf{r}_{aq} = \mathbf{a}_a - \mathbf{q}_q$ between the points in the two domains, and $G(r_{aq}, \omega)$ is the free space Green’s function as described in Equation (10), which decays with the increase of the distance r_{aq} and of ω , as in Table 1.

The surface normal velocities in the frequency domain can be taken from the 3D velocities of Equation (6). They are linked to the dynamic out-of-plane displacements over the static configuration \mathbf{q} , by means of the relation $v_n(\mathbf{q}, \omega) = -i\omega d_n(\mathbf{q}, \omega)$, which are expressions, by $d_n(\mathbf{q}, \omega) = \mathbf{H}_{d_nqf}(\omega) \cdot \mathbf{F}_f(\omega)$, of the receptance FRFs $\mathbf{H}_{d_nqf}(\omega)$ of size $N_q \times N_f$ (N_q being the number of outputs and N_f of inputs) and of the excitation signatures $\mathbf{F}_f(\omega)$. Equation (10) can therefore be rewritten taking advantage of the receptance FRFs, being analytical, numerical or experiment-based:

$$p(\mathbf{a}_a, \omega) = -2\omega^2\rho_0 \int_S \mathbf{H}_{d_nqf}(\omega) \mathbf{F}_f(\omega) G(r_{aq}, \omega) dS \in \mathbb{C}, \tag{11}$$

with $\mathbf{H}_{d_nqf}(\omega)$, $\mathbf{F}_f(\omega)$ and $G(r_{aq}, \omega)$ as complex-valued quantities, therefore also $p(\mathbf{a}, \omega) \in \mathbb{C}$. Note that normally \mathbf{r}_{aq} are considered as constant and real-valued vectors. It might be noted, instead, that \mathbf{r}_{aq} may become $\hat{\mathbf{r}}_{aq}(\omega) = \mathbf{a} - \mathbf{q} - \mathbf{H}_{d_nqf}(\omega) \cdot \mathbf{F}_f(\omega)$, thus complex-valued. Nonetheless, being the contributions $\mathbf{H}_{d_nqf}(\omega) \cdot \mathbf{F}_f(\omega)$ of at least 3 orders of magnitude lower than the static distances \mathbf{r}_{aq} when far enough from the sound pressure source, they can be neglected at first approximation ($\hat{\mathbf{r}}_{aq} \approx \|\mathbf{r}_{aq}\| = \|\mathbf{a}_a - \mathbf{q}_q\|$), as well as the infinitesimal surface deflection that pumps in a direction slightly different from the actual normal, with clear computational advantages.

If the vibrating surface domain S that generates the sound pressure can be discretised as $S \approx \sum_q \Delta S_q$, with ΔS_q as the discrete rectangular area of the surface with q -th point as centroid and dimensions as an average of the distances from the neighbouring points in the grid, Equation (11) can be expressed in terms of a sum of discrete contributions instead of an integral:

$$p(\mathbf{a}_a, \omega) \approx -2\omega^2\rho_0 \sum_q^{N_q} \mathbf{H}_{d_nqf}(\omega) \mathbf{F}_f(\omega) G(r_{aq}, \omega) \Delta S_q \in \mathbb{C}. \tag{12}$$

Note that the accuracy of this discretisation increases with the spatial definition of the receptance FRFs, as will be proved in the following section, by means of experiment-based full-field receptances, especially as $N_q > 1000$.

Being $G(r_{aq}, \omega)$ and ΔS_q functions of the locations of the N_a points in the acoustic domain and of the N_q points on the radiating structure, they can be grouped in a *complex-valued collocation matrix* $\mathbf{T}_{aq}(\omega)$, sized $N_a \times N_q$, of single element $T_{aq}(\omega) = -2\rho_0 G(r_{aq}, \omega) \Delta S_q$, to compact, by matrix algebra, Equation (12) into:

$$p(\mathbf{a}_a, \omega) \approx \omega^2 \mathbf{T}_{aq}(\omega) \mathbf{H}_{d_n q f}(\omega) \mathbf{F}_f(\omega) \in \mathbb{C}. \quad (13)$$

If, as the *acoustic transfer vectors* in [2,3], an *acoustic transfer matrix* $\mathbf{V}_{aq}(\omega)$, also callable *vibro-acoustic FRFs*, is defined as:

$$\mathbf{V}_{aq}(\omega) = \omega^2 \cdot \mathbf{T}_{aq}(\omega) \cdot \mathbf{H}_{d_n q f}(\omega) \in \mathbb{C}, \quad (14)$$

Equation (13) becomes:

$$p(\mathbf{a}_a, \omega) \approx \mathbf{V}_{aq}(\omega) \mathbf{F}_f(\omega) \in \mathbb{C}. \quad (15)$$

The *collocation matrix* $\mathbf{T}_{aq}(\omega)$ allows the estimation of the pressure field by means of matrix multiplications, which are made just bigger (asking for increased computational resources) in the case of finer grids in both the acoustic and structural domains.

By means of the *smoothed receptance matrix* $\hat{\mathbf{H}}_{d_j}(\omega)$ in Equation (2), a *smoothed pressure* $\hat{p}(\mathbf{a}_a, \omega)$ can be evaluated either from Equation (13) or (15), specifically as:

$$\hat{p}(\mathbf{a}_a, \omega) \approx \omega^2 \mathbf{T}_{aq}(\omega) \hat{\mathbf{H}}_{d_n q f}(\omega) \mathbf{F}_f(\omega) \in \mathbb{C}, \quad (16)$$

$$\hat{p}(\mathbf{a}_a, \omega) \approx \hat{\mathbf{V}}_{aq}(\omega) \mathbf{F}_f(\omega) \in \mathbb{C}, \quad (17)$$

where the *smoothed acoustic transfer matrix* $\hat{\mathbf{V}}_{aq}(\omega)$ becomes:

$$\hat{\mathbf{V}}_{aq}(\omega) = \omega^2 \cdot \mathbf{T}_{aq}(\omega) \cdot \hat{\mathbf{H}}_{d_n q f}(\omega) \in \mathbb{C}. \quad (18)$$

Analogously to Equation (3), a *pressure error function* $e_p(\mathbf{a}_a, \omega)$ and an *acoustic transfer matrix error function* $e_{\mathbf{V}_{aq}}(\mathbf{a}_a, \omega)$ can be defined as:

$$e_p(\mathbf{a}_a, \omega) = p(\mathbf{a}_a, \omega) - \hat{p}(\mathbf{a}_a, \omega) \approx \omega^2 \mathbf{T}_{aq}(\omega) [\mathbf{H}_{d_n q f}(\omega) - \hat{\mathbf{H}}_{d_n q f}(\omega)] \mathbf{F}_f(\omega) \in \mathbb{C}, \quad (19)$$

$$e_{\mathbf{V}_{aq}}(\mathbf{a}_a, \omega) = \mathbf{V}_{aq}(\omega) - \hat{\mathbf{V}}_{aq}(\omega) = \omega^2 \cdot \mathbf{T}_{aq}(\omega) \cdot [\mathbf{H}_{d_n q f}(\omega) - \hat{\mathbf{H}}_{d_n q f}(\omega)] \in \mathbb{C}. \quad (20)$$

Equation (15) can be relevant when the structural response and acoustic domains are kept constant (meaning the *acoustic transfer matrix* $\mathbf{V}_{aq}(\omega)$ is unchanged), while varying the excitation signature, to map the effect of different structural responses on the acoustic pressure field. Note also that Equations (13)–(15) allow the calculation of the sound pressure field directly from *experiment-based full-field receptances*, which should help the accuracy of the results. The latter can be achieved thanks to the high spatial resolution of the full-field *receptances* and because these *receptances*, being evaluated directly from the test, retain the true blending of any *complex-valued* modeshape, active at the specific frequency and phase delay, with the proper real boundaries and dissipation/damping effects of the actual vibrating structure.

2.4. Comparative Tools

In order to quantify the differences among the *vibro-acoustic FRF maps* due to the potential errors on the *raw receptances*, some mathematical tools should be recalled, as in [33] and Appendix B of [34], from the suggestions in [62].

2.4.1. Modal Assurance Criterion

MAC can be applied to the entire fields of two sets to address the overall similarity among the different datasets at a specific couple of frequencies, instead of modes. MACii looks at the diagonal results of the MAC matrix, with emphasis on the comparison of the

whole fields at a single common frequency. MAC matrices and MACii functions can thus assess the similarities in the whole spectral domain. Therefore MAC and MACii functions can be here extended to two distinct sets of any type of full-field FRFs, being FRFs' maps of homogeneous quantities (*receptances* or *vibro-acoustic FRFs* ($\mathbf{H}_a, \mathbf{H}_b$) pairs), as:

$$MAC_{\omega_1, \omega_2} = \frac{|\mathbf{H}_a(\omega_1)\mathbf{H}_b^H(\omega_2)|^2}{\mathbf{H}_a(\omega_1)\mathbf{H}_a^H(\omega_1)\mathbf{H}_b(\omega_2)\mathbf{H}_b^H(\omega_2)} \in [0, 1] \tag{21}$$

$$MACii_{\omega} = \frac{|\mathbf{H}_a(\omega)\mathbf{H}_b^H(\omega)|^2}{\mathbf{H}_a(\omega)\mathbf{H}_a^H(\omega)\mathbf{H}_b(\omega)\mathbf{H}_b^H(\omega)} \in [0, 1] \tag{22}$$

where $()^H$ is the *hermitian* operator.

2.4.2. Frequency Response Assurance Criterion

FRAC can instead highlight where on the maps the dofs correlate better in the whole frequency range, giving a geometry-dependent comparative result, which can also be seen as a comparative pattern.

$$FRAC_{ij} = \frac{\left| \sum_{\omega=\omega_{start}}^{\omega_{end}} H_{a_{ij}}(\omega)H_{b_{ij}}^H(\omega) \right|^2}{\sum_{\omega=\omega_{start}}^{\omega_{end}} H_{a_{ij}}(\omega)H_{a_{ij}}^H(\omega) \sum_{\omega=\omega_{start}}^{\omega_{end}} H_{b_{ij}}(\omega)H_{b_{ij}}^H(\omega)} \in [0, 1] \tag{23}$$

2.4.3. Signal-to-Noise Ratio

Beside the above functions, standard statistical analysis [53] can be performed, to extract the maximal *max*, the minimal *min*, the average *mean*, the standard deviation *Std.Dev.* values. From them, a signal-to-noise ratio *snr* can be calculated as:

$$snr = mean/Std.Dev. \in \mathbb{R} \tag{24}$$

3. Results

Keeping in mind the aim of this paper—that of finding how the errors on the experiment-based *receptances* are spread into the vibro-acoustic simulations—it becomes relevant to build and comment, with the tools outlined in Section 2, a bunch of simulations, carried out at increasing distances from the vibrating plate, using *raw receptances* and *smoothed receptances*. Since the pressure in Equation (15), given a known excitation, is influenced only by the potential errors in the *acoustic transfer matrix* $V_{aq}(\omega)$, the focus will be on the latter, disregarding Equations (16), (17) and (19). Therefore *raw* and *smoothed* versions of the *receptance matrices* of Equations (1) and (2), and of the *acoustic transfer matrix* of Equations (14) and (18), at different distances will be proposed. The errors on the *receptances* were isolated in Equation (3), whereas those on the *acoustic transfer matrix* in Equation (20). Starting from the description of these simulations, the errors' effects will be followed, analysed in type and commented on in two meaningful examples as per the error's type.

3.1. Sound Pressure Mapping from Full-Field Receptances

As just highlighted above in Section 2.3, the distributed motion on the sound radiating surface can be modelled by means of the *experiment-based full-field receptances* obtained from Sections 2.1 and 2.2. In particular, from Equation (15), it is clear how relevant the evaluation of the defined *acoustic transfer matrix* $V_{aq}(\omega)$ becomes, in order to simulate how the excitation force—acting on a specific location on the plate—can be transferred to the acoustic pressure in the acoustic domain.

In each picture of the simulated *acoustic transfer matrix* $V_{aq}(\omega)$ appears the label “Acoustic Pressure/N” to state the type of quantity, followed by “RR” for *Raw Receptance*

source, or “SR” for *Smoothed Receptance*; the endings “r” or “_r” and “s” or “_s” are used with the same meaning. When visible, the active shaker is highlighted in yellow with a big dot at the corresponding structural location, while for the mute shaker the chosen color is grey. The highlighted magenta dot pertains to the dof of interest, in the structural domain for the *receptances*, but instead in the acoustic mesh for the *acoustic transfer matrix*. All the quantities retain their *complex valued* nature, with the projection angle fixed to 0 in the 3D pictures for proper comparison, whereas complex amplitude and phase are used in the 2D charts. Instead, *real-valued* quantities from the comparative tools in Section 2.4 display only the amplitude. Specific function values in the magenta acoustic dof and extrema are inserted where needed. In the 2D charts a vertical yellow line follows the frequency line of interest (also highlighted with a text label), whereas the horizontal line follows the value of the specific function, with similar color tone. The label “References: Geom SLDV Freq SLDV”, according to [14], means no transformations were applied to the acquired *raw receptance* from the SLDV technique, thus used without any numerical errors coming from interpolation schemes. The axes triad in Figure 2a–d shows the out-of-plane direction Z from the structural domain towards the acoustic mesh, therefore spatially and virtually located in front of the measured surface, towards the instruments of Figure 1a,b.

3.1.1. Meshing the Acoustic Domain

For the proof-of-concept of what introduced, a simple 3D acoustic domain meshing routine was prepared. Different geometries are available in it for meshing the acoustic grid (flat rectangle, part of a cylinder, part of a sphere), as the discrete locations of the virtual pressure receivers that can be freely positioned in the 3D space, relative to the radiating surface. The flat rectangular grid was chosen, as exemplified in the back-side view of Figure 2, with different positioning for the discussion of the results at increasing distances.

The number of nodes in the grid has no specific limit in the meshing routine, except for computational burden, if the acoustic simulation evaluates serially, for each frequency line, the positioning vectors r_{aq} for the *complex-valued collocation matrix* $T_{aq}(\omega)$. As an alternative to a serialised calculation, slower but less demanding in terms of RAM allocation, a parallel computing strategy was optimised (limited to use up to 51×51 nodes in the acoustic grid and 145 GB of RAM; the *experiment-based receptances* are obtained in a grid of 57×51 dofs ($N_q = 2907$) and 1285 frequency lines) on the computing environment available (based on C-language OpenMP code, gcc 7.5.0 in OpenSUSE[®] Linux environment, and on a workstation with 192 GB of RAM, 12 physical cores in dual hexacore Intel[®] Xeon[®] X5690 CPUs running at 3.46–3.73 GHz) to take advantage of the common positioning vectors r_{aq} in the Green’s functions and in Equations (12)–(15), between structural and acoustic domains; the r_{aq} may be evaluated, in parallel among the threads, just once and kept allocated afterwards in memory for each frequency line, in the acoustic field approximations made at the same distance. Therefore, in this paper a rectangular mesh of size 500 mm \times 500 mm was prepared, with 51×51 dofs ($N_a = 2601$, 10 mm among each dof), centred on the vibrating plate and positioned at four different distances [25 mm, 75 mm, 150 mm, 300 mm] above it as displayed in Figure 2; this grid size was chosen to speed up the calculations with the parallel computing routines as mentioned above, while keeping a very high meshing resolution. The parameters of the medium (air) were fixed in $c_0 = 300.0$ m/s and $\rho_0 = 1.204$ kg/m³.

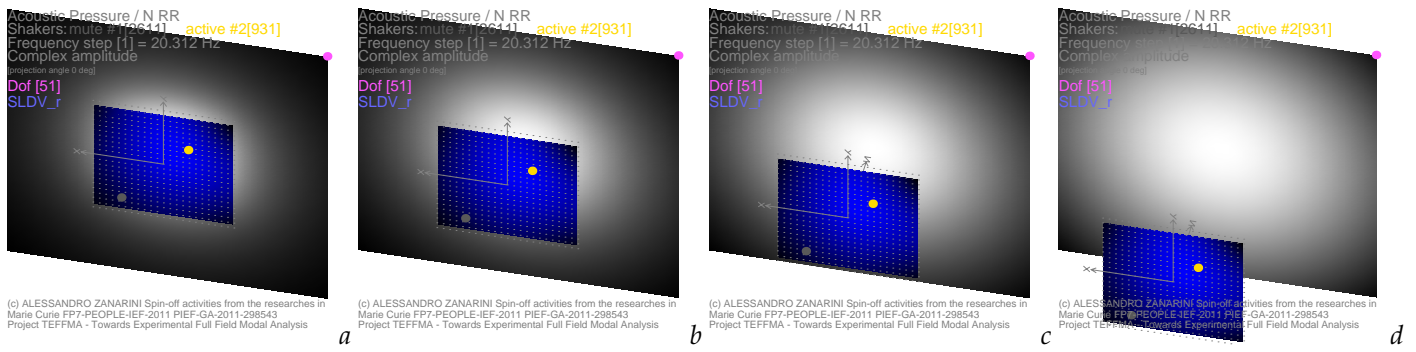


Figure 2. Relative position of the radiating surface (in blue tones) and the acoustic domain of interest (in grey tones), at specific distances of 25 mm in (a), of 75 mm in (b), of 150 mm in (c) and of 300 mm in (d), excitation from shaker 2 (in the yellow dot) at 20 Hz.

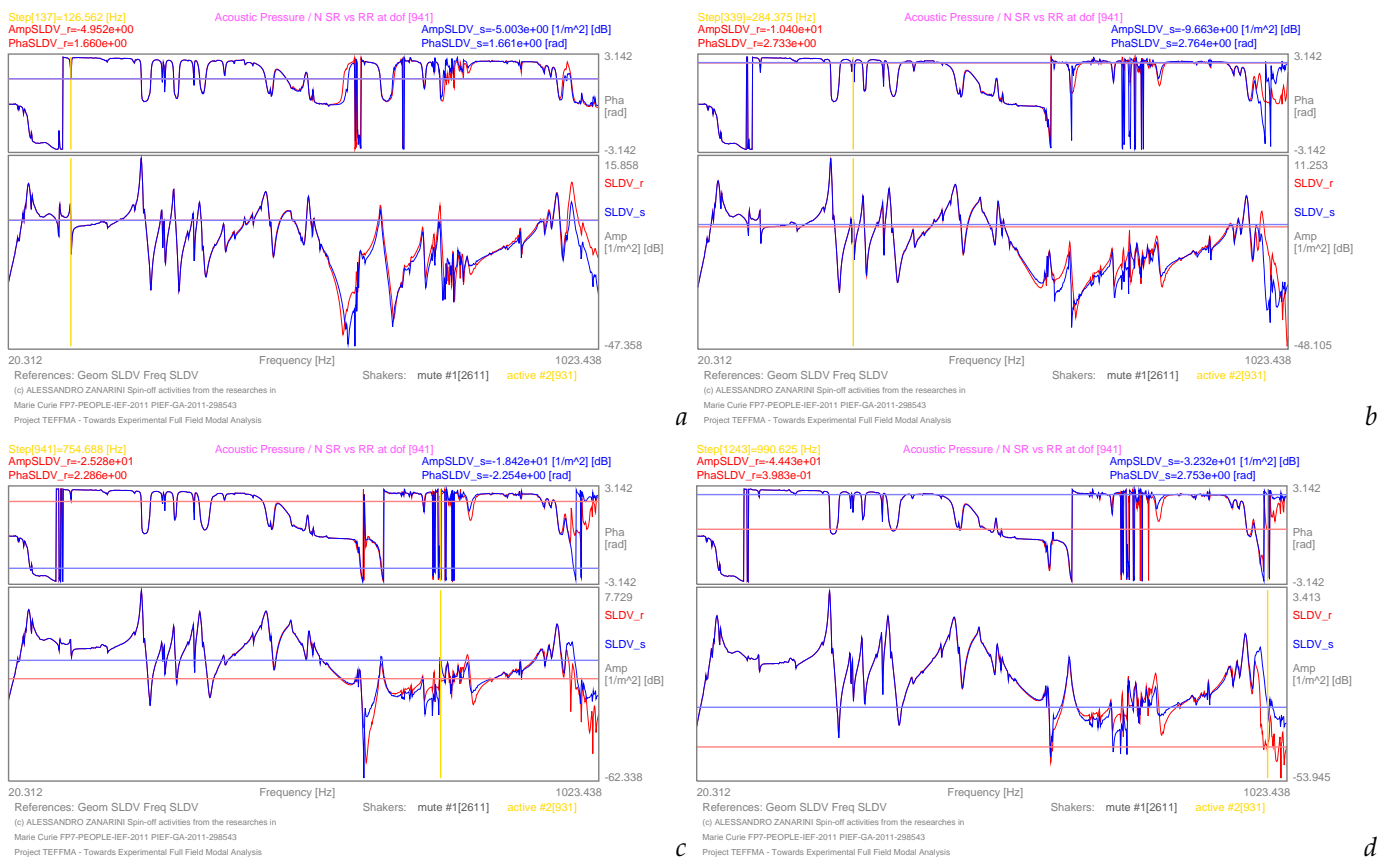


Figure 3. Vibro-acoustic FRFs in acoustic dof 941, obtained in Equations (14) and (18) from raw (red) and smoothed (blue) receptances respectively, in the [20–1024] Hz frequency range at specific distances of 25 mm (a), of 75 mm (b), of 150 mm (c) and of 300 mm (d) from shaker 2 in structural dof 931.

3.1.2. Notes about the Evaluation of the Acoustic Transfer Matrix

One of the paper’s aims is to evaluate the acoustic transfer matrix $V_{aq}(\omega)$ in Equation (14), or vibro-acoustic FRFs (as acoustic pressure over force), directly from the experiment-based receptances in Equation (1), as proposed in Section 2.3, without the need of any FE structural model, but with great spatial and frequency domains’ details and inherent field quality, especially regarding the lack of assumptions and of approximations about the real structure. As Sections 2.1 and 2.2 highlighted, accurate receptance matrices $H_{a_n,qf}(\omega)$ were estimated with high resolution in spatial and frequency domains from both shakers available in the TEFfMA project, with the SLDV as the reference for the topology

of the geometry and for the frequency domain [34]. In Figure 3 examples of *vibro-acoustic FRFs* are reported from both the *raw* (*_r, in red) and *smoothed* (*_s, in blue) *receptances* by using Equations (14) and (18), as a frequency domain relation from the force of shaker 2 in structural dof 931 and the acoustic pressure in acoustic dof 941, whose position is highlighted by a magenta dot in Figure 4. Shaker 2 was selected because it provided the noisiest *raw receptances* among the two shakers available in the measurement campaign [11–14]. Great attention should be paid to the dense dynamics in the *vibro-acoustic FRFs* from Equations (14) and (18) of Figure 3. This dense dynamics is inherited from the high quality *complex-valued full-field receptances* in Equations (1) and (2), with or without the smoothing, not only of the amplitude's, but also of the phase's information, confirming what was proposed in Section 2.3. The examples of the *acoustic transfer matrix* single dof graph shown in Figure 3a come from the simulation taken at 25 mm from the vibrating surface, those in Figure 3b at 75 mm, in Figure 3c at 150 mm, and in Figure 3d at 300 mm. This was done to highlight the variability of the *vibro-acoustic FRFs* according to the distance (see Equation (10) and Table 1), as it is reflected both in terms of *vibro-acoustic FRF extremes* (here in dB), in terms of acoustic shapes and blending of components. Special attention was paid to the *complex-valued* nature of the quantities (*amplitude* and *phase*), which also vary along the mesh, as will be later shown in the *vibro-acoustic patterns* at specific frequencies.

Again it is of relevance how the *acoustic transfer matrix*—obtained from the *experiment-based receptances*—preserves, with its *complex-valued* nature, the real life conditions of the test, without any simplification in the material properties, damping and boundaries, nor in the modal base truncation or identification that are not needed.

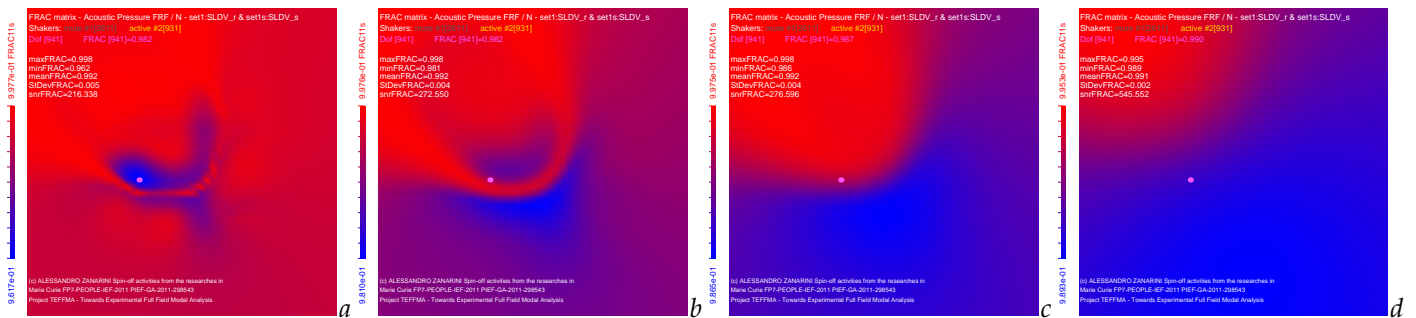


Figure 4. FRAC mapping between *raw acoustic transfer matrix* in Equation (14) and *smoothed acoustic transfer matrix* in Equation (18) at specific distances of 25 mm in (a), of 75 mm in (b), of 150 mm in (c) and of 300 mm in (d) from shaker 2, with the statistics in Table 2.

Table 2. FRAC statistics of the comparison between *vibro-acoustic maps* of Equations (14) and (18), obtained from *raw* and *smoothed* optical full-field *receptances* in Equations (1) and (2).

Distance	Max	Min	Mean	Std.Dev.	snr
25 mm	0.998	0.962	0.992	0.005	216.338
75 mm	0.998	0.981	0.992	0.004	272.550
150 mm	0.998	0.986	0.992	0.004	276.596
300 mm	0.995	0.989	0.991	0.002	545.552

3.1.3. Revealing Error Effects by Means of the FRAC Matrices

As said in Section 2.4, FRAC matrices in Equation (23) are used here to determine the sum of differences in the vibro-acoustic FRF simulations, related to the spatial-, or mesh-, domain. These differences are due to the use of *raw* and *smoothed receptances* as the source in the simulations of the sound radiation in the whole frequency domain. Specifically, Figure 4a–d reports this FRAC mapping with varying distance from the vibrating plate. Table 2 highlights the statistics of the depicted FRAC patterns. Although the FRAC mapping in Figure 4a, with the acoustic mesh at merely 25 mm above the vibrating plate, is heavily characterised by the complexity of the underneath shapes in the *receptances*, like in the nearfield acoustic holography (NAH, see e.g., [48,61,63,64]), as the distance—between the acoustic mesh and the plate—grows, the vibro-acoustic simulations appear to be progressively less sensitive to the diversities between the *raw* and *smoothed receptances*. Figure 4b follows with a smoother shape, as well as Figure 4c has lost the central bold ridge, while Figure 4d appears more like a large-radius dome. This is also appreciated in the FRAC statistics' data in Table 2: the comparisons show a minimal *min* value that increases with the distance, while the *mean* remains essentially the same, as the sources are detached by only minimal discrepancies due to the smoothing applied, as will be better explained further in this paper. The *Std.Dev.* instead decreases, highlighting the higher uniformity (or larger curvature) of the FRAC matrix, together with an increasing *snr*.

3.1.4. Revealing Error Effects by Means of the MACii Functions

Table 3 gives the statistics of the global comparative MACii functions of Equation (22), introduced in Section 2.4 to determine potential differences in the vibro-acoustic FRF simulations of Equations (14) and (18), across the whole frequency domain of interest; the statistics can be extracted from any of the MACii graphs proposed, precisely from Figures 6, 11, 16, 21, 26 and 31. The minimal value achieved by the MACii functions is affected by the distance at which the vibro-acoustic simulation is run, especially in the mid-range of 75–150 mm, whereas at 300 mm the blending of all the discrepancies helps raise the comparison's values. The *mean* of the MACii functions increases with the distance of the acoustic field from the vibrating plate, except for the evaluation at 75 mm. Conversely, the *standard deviation* lowers, but not at 75 mm. All this brings an *snr* with a minimum of 12.65 at 75 mm, but increasing values from that of 17.33 at 25 mm, passing to a similar 18.06 at 150 mm, until the highest value of 31.12 at 300 mm is reached, underling the role of the distance from the vibrating plate as a mitigation of discrepancies in the fields, which look more uniform and comparable with or without the applied smoothing.

At the same time, the statistics of Table 3 do not tell us much about diversities among noise fields. But it is clear how there are regions in the MACii functions where the drops in the comparison are localised and where deeper investigation is needed, as follows.

Table 3. MACii statistics of the comparison between vibro-acoustic maps of Equations (14) and (18), obtained from *raw* and *smoothed* optical full-field *receptances* in Equations (1) and (2).

Distance	Max	Min	Mean	Std.Dev.	snr
25 mm	1.000	0.680	0.978	0.056	17.329
75 mm	1.000	0.402	0.976	0.077	12.647
150 mm	1.000	0.389	0.986	0.055	18.064
300 mm	1.000	0.605	0.993	0.032	31.116

Table 4. MACii values at specific frequencies of the comparison between vibro-acoustic maps of Equations (14) and (18), obtained from *raw* and *smoothed* optical full-field *receptances* in Equations (1) and (2).

Distance	127 Hz	250 Hz	284 Hz	336 Hz	755 Hz	991 Hz
25 mm	1.000	1.000	0.988	0.962	0.796	0.703
75 mm	1.000	1.000	0.994	0.994	0.686	0.411
150 mm	1.000	1.000	0.998	0.999	0.617	0.459
300 mm	1.000	1.000	0.999	1.000	0.801	0.605

If the *raw* and *smoothed receptance* shapes, varying with frequency, are taken into account together with the MACii functions, it appears instead that the drops in MACii values are related to the noise, or errors, onto those shapes. Specifically, as will be discussed later, three different noise patterns can be identified: uniformly-distributed noise, measurement-system-related noise and filtering-related noise. For each of them, two exemplifying behaviours are discussed below in the next Sections 3.2–3.4, at their respective frequency pairs: 127 and 250 Hz for the uniformly-distributed noise, 284 and 336 Hz for the measurement-system-related noise, and 755 and 991 Hz for the filtering-related noise. Table 4 summarises the impact of the error type on the global comparison by means of MACii results, at specific frequencies as discussed below, when the graphs will also be introduced as Figures 6, 11, 16, 21, 26 and 31. In Table 4 it appears clear how the uniformly distributed noise has no influence on the MACii values, therefore how MACii functions are not able to detect this type of noise on the *receptances*. When the noise has a specific pattern superimposed onto the ODS, which is not uniformly distributed and hard to be predicted by noise models, but instead is related only to the real measurements, or measurement system, the MACii functions can instead show some alarms. Again the latter fade away with the increasing distance from the vibrating plate (see Equation (14) and Table 1), thus confirming how local behaviours, with associated low energy, are sensed only by the acoustic domain when close to the radiating surface. Instead, when the action of filtering attempts to overly smooth high-order patterns of measurement-related disturbances, reducing the *receptances'* amplitudes and thus the emitted sound energy, the MACii functions clearly reveal the discrepancy between the simulations, run with the *raw receptances* and the *smoothed receptances*, particularly at the medium distances, like at 75 and 150 mm, but also strongly manifest at close and far fields. It might also be noted in the examples of Figure 3a–d that the measurement-related patterns of noise are, with or without filtering distortions, more relevant in magnitude as the frequency raises, compared to the declining amplitudes in the *receptances*.

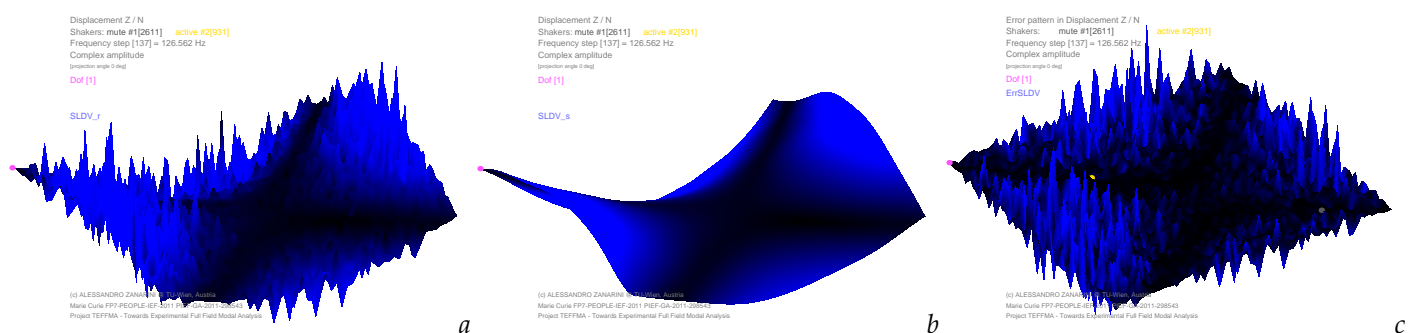


Figure 5. Examples of *receptance shapes* with their experiment-related noise (in (a), Equation (1)) against the smoothed version (in (b), Equation (2)) and related error pattern (in (c), Equation (3)) at the specific frequency of 127 Hz, excitation from shaker 2.

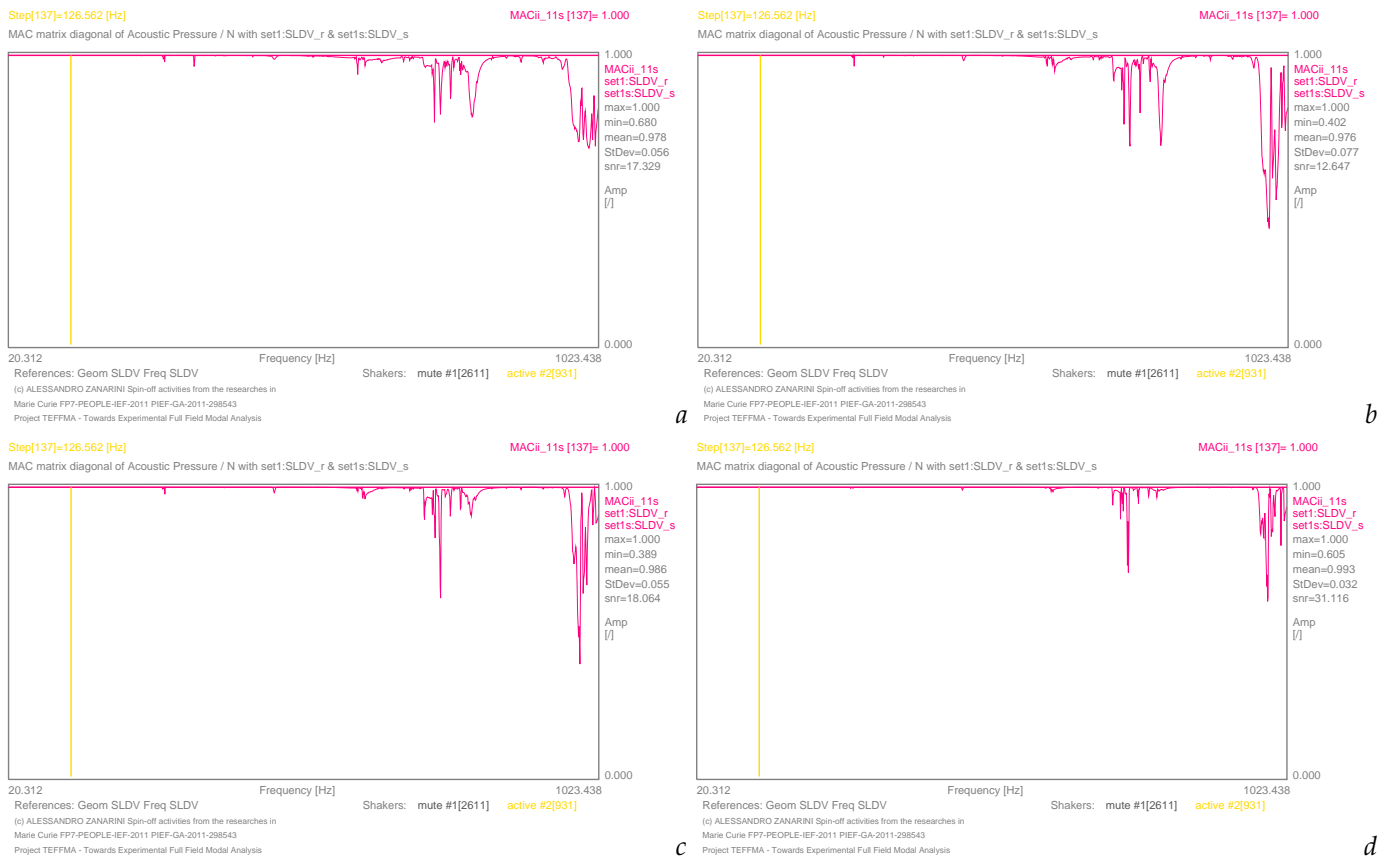


Figure 6. MACii graphs in the comparison of the *acoustic transfer matrix* as in Equations (14) and (18), at specific distances of 25 mm in (a), 75 mm in (b), 150 mm in (c), and 300 mm in (d) at the specific frequency of 127 Hz, with excitation from shaker 2.

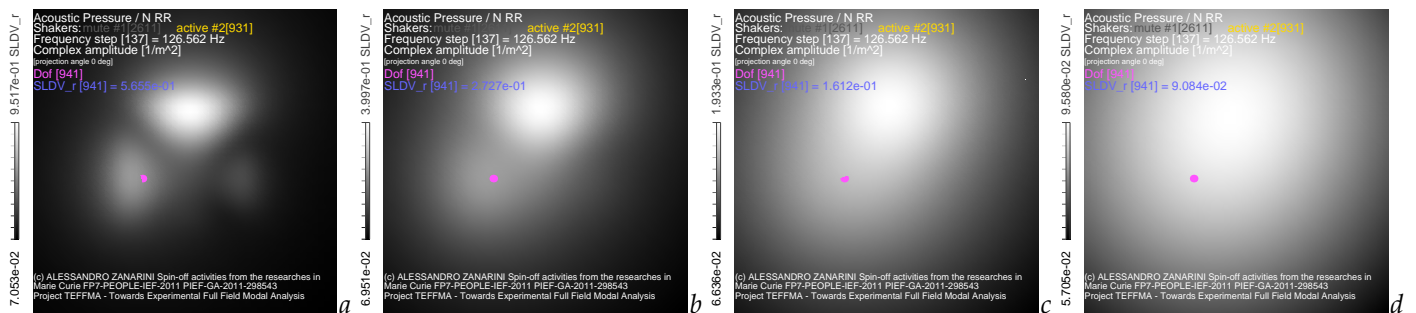


Figure 7. Vibro-acoustic FRF mapping of Equation (14) from *raw receptances* in Equation (1) at 127 Hz at specific distances of 25 mm in (a), of 75 mm in (b), of 150 mm in (c) and of 300 mm in (d) from shaker 2.

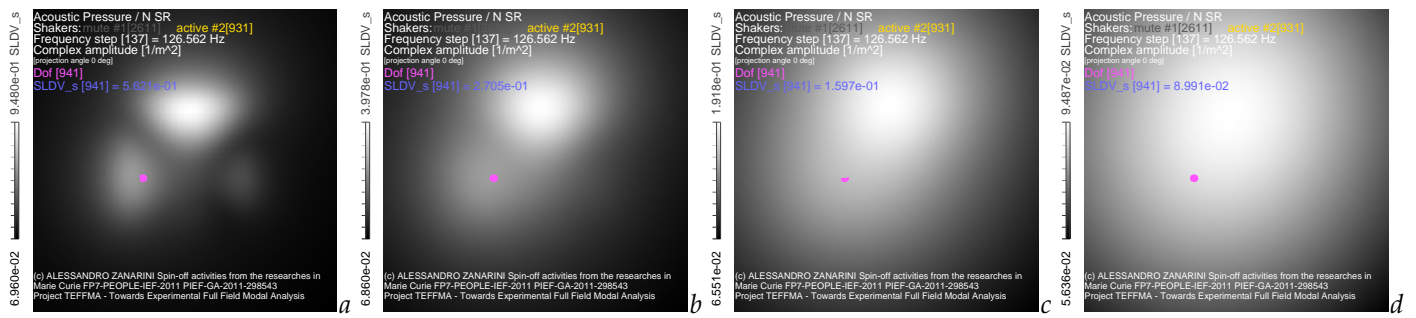


Figure 8. Vibro-acoustic FRF mapping of Equation (18) from *smoothed receptances* in Equation (2) at 127 Hz at specific distances of 25 mm in (a), of 75 mm in (b), of 150 mm in (c) and of 300 mm in (d) from shaker 2.

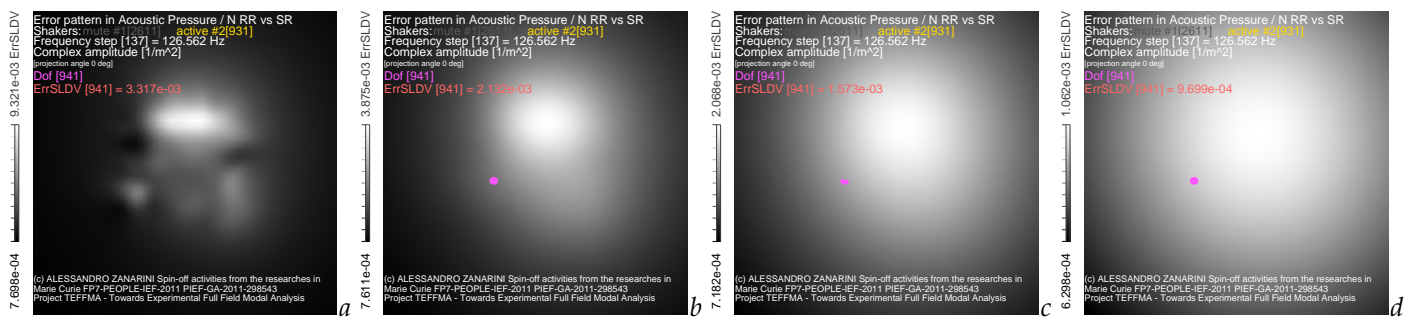


Figure 9. Error patterns of Equation (20) in vibro-acoustic FRF mapping from *experiment-based receptances* at 127 Hz at specific distances of 25 mm in (a), of 75 mm in (b), of 150 mm in (c) and of 300 mm in (d) from shaker 2.

3.2. Uniformly Distributed Amplitude-Modulated Noise Effects

The first type of error on the *receptance matrix* of Equation (1) that is normally addressed (see also the comments in Section 1 about the presentation of [10]) is that of a uniform distribution, which is not found here. Here, in real measurements instead, the noise distribution of Equation (3) needs to be extended to a *complex-valued* amplitude-modulated nature, over the entire spatial field of the *receptances*. This amplitude-modulation effect, due to the specific ODS, amplifies the noise distribution in the most deflected areas, whereas it reduces the noise close to the nodal lines. Figure 5a depicts the noisy *raw receptance* map at the frequency of 127 Hz from Equation (1), whereas Figure 5b shows the same shape once it is smoothed by a shifting polynomial filter [33,34,65], tuned to low-order complexity of the shapes to lower the errors iteratively as in Equation (2). Figure 5c isolates the experiment-based error pattern of the *raw receptance* as in Equation (3). A similar trend is shown in Figure 10a–c at 250 Hz. In both Figures 5 and 10 the noise is indeed modulated by the amplitude magnitude of the corresponding ODS, with noise peaks on the most deflected parts of the maps, whereas the noise is hardly distinguishable on the black areas close to the nodal lines, where the ODS exhibits minimal or null displacement over excitation force, thus limited modulation. Although the noise on the *raw receptance* seems quite relevant in terms of amplitude, relative to the smoothed ODS including stochastic phase scattering, the same can not be said as affecting the vibro-acoustic simulations of Equations (14) and (18), run from the same *raw* and *smoothed receptances*; also the unitary MACii values confirm it in Table 4, Figures 6 and 11 at every distance. As the discussion above in Section 3.1.4 hinted, this type of noise was hard to be revealed in the comparison with a noise-free source. This can be a partial, or amplitude-modulated noise-type-dependant, confirmation of the comments about uniformly distributed noise in [10].

Table 5. Ranges of complex amplitude [$1/m^2$] and the ratio of the extremes in the vibro-acoustic FRF fields—evaluated from the *raw receptances* in Equation (14), from the *smoothed receptances* in Equation (18)—and in the error function in Equation (20), at the specific frequency of 127 Hz.

Distance	Raw Max	Raw Min	Raw Ratio	Smooth Max	Smooth Min	Smooth Ratio	Err. Max	Err. Min	Err. Ratio
25 mm	9.517e-01	7.053e-02	13.49	9.480e-01	6.960e-02	13.62	9.321e-03	7.698e-04	12.11
75 mm	3.997e-01	6.951e-02	5.75	3.978e-01	6.860e-02	5.80	3.875e-03	7.611e-04	5.09
150 mm	1.933e-01	6.636e-02	2.91	1.918e-01	6.551e-02	2.93	2.068e-03	7.182e-04	2.88
300 mm	9.580e-02	5.705e-02	1.68	9.487e-02	5.636e-02	1.68	1.062e-03	6.298e-04	1.69

Table 6. Value of the complex amplitude [$1/m^2$] of the vibro-acoustic FRF field in acoustic dof 941 from the *raw receptances* in Equation (14), from the *smoothed receptances* in Equation (18), from the error function in Equation (20), and the ratio between the same error and the raw-based values at the specific frequency of 127 Hz.

Distance	Raw Value	Smoothed Value	Error Value	Ratio Error/Raw
25 mm	5.655e-01	5.621e-01	3.317e-03	5.866e-03
75 mm	2.727e-01	2.705e-01	2.132e-03	7.818e-03
150 mm	1.612e-01	1.597e-01	1.573e-03	9.758e-03
300 mm	9.084e-02	8.991e-02	9.699e-04	1.068e-02

In Figure 7a–d the vibro-acoustic FRF field of Equation (14) is displayed in its complex amplitude at 127 Hz, with grey tones starting from black at the minimal value and ending in white at the maximal value, as simulated from the *raw receptances* of Equation (1), at the four distances of interest. It can be easily understood, as expected due to the free-space Green’s functions of Equation (10) and Table 1, how the closer the distance is, the stronger the resemblance of the *receptance map* in Figure 5a appears in the vibro-acoustic FRF map, as in the NAH [48,63,64], especially in Figure 7a, less in Figure 7b. However, as the acoustic mesh is at a distance of 150 mm in Figure 7c, the footprint of the *receptance map* fades into a more generic dome, whose curvature becomes even larger at the maximal distance simulated in Figure 7d. The same conclusions can be drawn at 250 Hz for Figure 12a–d, obtained from the *raw receptance* of Figure 10a; but now a stronger persistence of the *raw receptance* pattern is exhibited till 150 mm away from the vibrating plate.

Figure 8a–d presents the vibro-acoustic simulations of Equation (18) evaluated from the *smoothed receptance map* of Figure 5b at 127 Hz in Equation (2), with the same statements about the fading footprint of the *receptance map* as the distance increases. Analogously, Figure 13a–d displays the vibro-acoustic simulations evaluated from the *smoothed receptance map* of Figure 10b at 250 Hz, again with a more articulated pattern till Figure 13c.

Since the maps in Figure 8a–d are hardly distinguishable from those in Figure 7a–d, there is the need to isolate the corresponding error patterns of Equation (20), coming from the *complex-valued* difference between the simulations at 127 Hz obtained from the *raw* and *smoothed receptances*, as displayed in Figure 9a–d. A closer look at the error patterns tells us that, with this type of amplitude-modulated and uniformly distributed noise, the impact of the latter is mostly evident at very close distance as in Figure 9a, whereas from 75 mm in Figure 9b the error pattern starts to be more undefined. The same type of error patterns is extracted in Figure 14a–d at 250 Hz: this time the pictures are influenced more by the amplitude modulating *receptance* of Figure 10, showing asymmetry in the error dome of the vibro-acoustic simulations at the intermediate distances in Figure 14b,c.

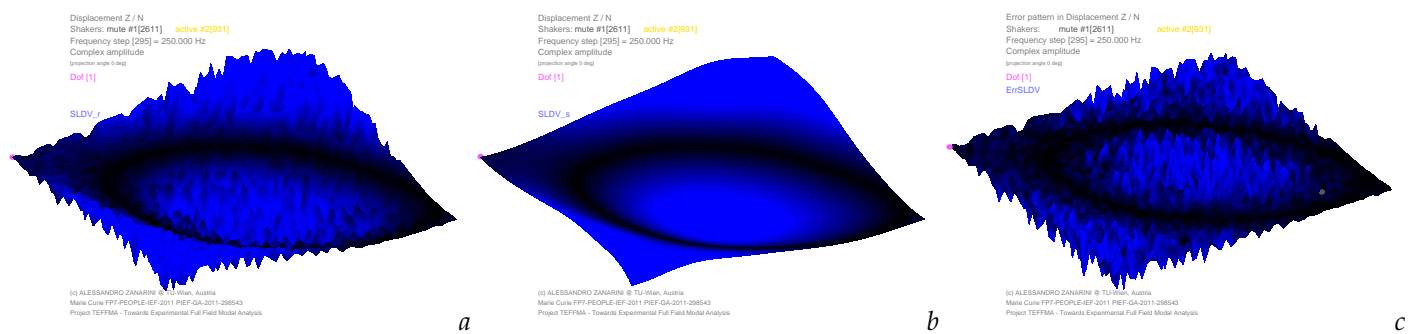


Figure 10. Examples of *receptance shapes* with their experiment-related noise (in (a), Equation (1)) against the smoothed version (in (b), Equation (2)) and related error pattern (in (c), Equation (3)) at the specific frequency of 250 Hz, with excitation from shaker 2.

Table 5 proposes the maximal values, the minimal values and their ratio of the vibro-acoustic FRF fields, coming from the *raw* and *smoothed receptances* at 127 Hz, together with those of the error pattern of Equation (20), coming from the *complex-valued* difference of the vibro-acoustic simulations. Discussing these ranges, and inherent ratios, can be useful to assess the simplicity—or flatness—of the vibro-acoustic FRF fields. Specifically, for this type of amplitude-modulated and uniformly distributed noise on the radiating source, it can be appreciated how at 127 Hz all the fields behave quite similarly, with the vibro-acoustic error patterns of two orders lower than the acoustic pressure over force in both the simulations, but with a very similar ratio, witness of a marginality of the structural dynamics' noise on the acoustic field. Instead, at 250 Hz, Table 7 describes a slightly different behaviour, with a much stronger ratio of the ranges, especially at lower distances. The same type of data distribution is not repeated among the simulations evaluated from *raw* and *smoothed receptances* in Equations (14) and (18), thus highlighted by the error patterns of Equation (20). Table 7 underlines the above mentioned difference, in particular at 25 and 75 mm away from the plate; also at 150 mm the error pattern has a different complex amplitude distribution than the simulations, which is more regular only at 300 mm.

If the complex amplitude of the vibro-acoustic FRF is evaluated in a specific dof of the acoustic mesh, here the dof 941 located in the magenta dot of the maps in Figures 7–9 at 127 Hz, or in Figures 12–14 at 250 Hz, a punctual error evaluation, together with the ratio between the error and the simulation from *raw receptance*, can be run, as in Table 6 at 127 Hz or in Table 8 at 250 Hz. Dof 941 was selected as being close to the ridge and in a depression area of the FRAC matrix in Figure 4a, as a potential dof where the noise on the *receptances* could have more influence on the *acoustic transfer matrices*. In Figure 3 the vibro-acoustic FRFs of Equations (14) and (18), obtained from the *raw* and *smoothed receptances*, are compared, showing minimal error impact especially at 127 Hz in the near field (Figure 3a). Table 6 confirms the most regular behaviour, and lower noise influence, found at 127 Hz, which means a slight increase in the marginal error ratio—although roughly restrained into 1%—with the distance of the acoustic mesh from the vibrating plate. Indeed, Table 8 at 250 Hz highlights higher (roughly double) error ratios on the punctual function, as soon as the distance is increased, from 75 mm to 300 mm. Therefore, the *receptances* of Figure 10 have a bit stronger effect in distorting the vibro-acoustic simulations, thanks to a different *smoothed receptance* and the related energy content in the amplitude-modulation of the uniformly distributed noise.

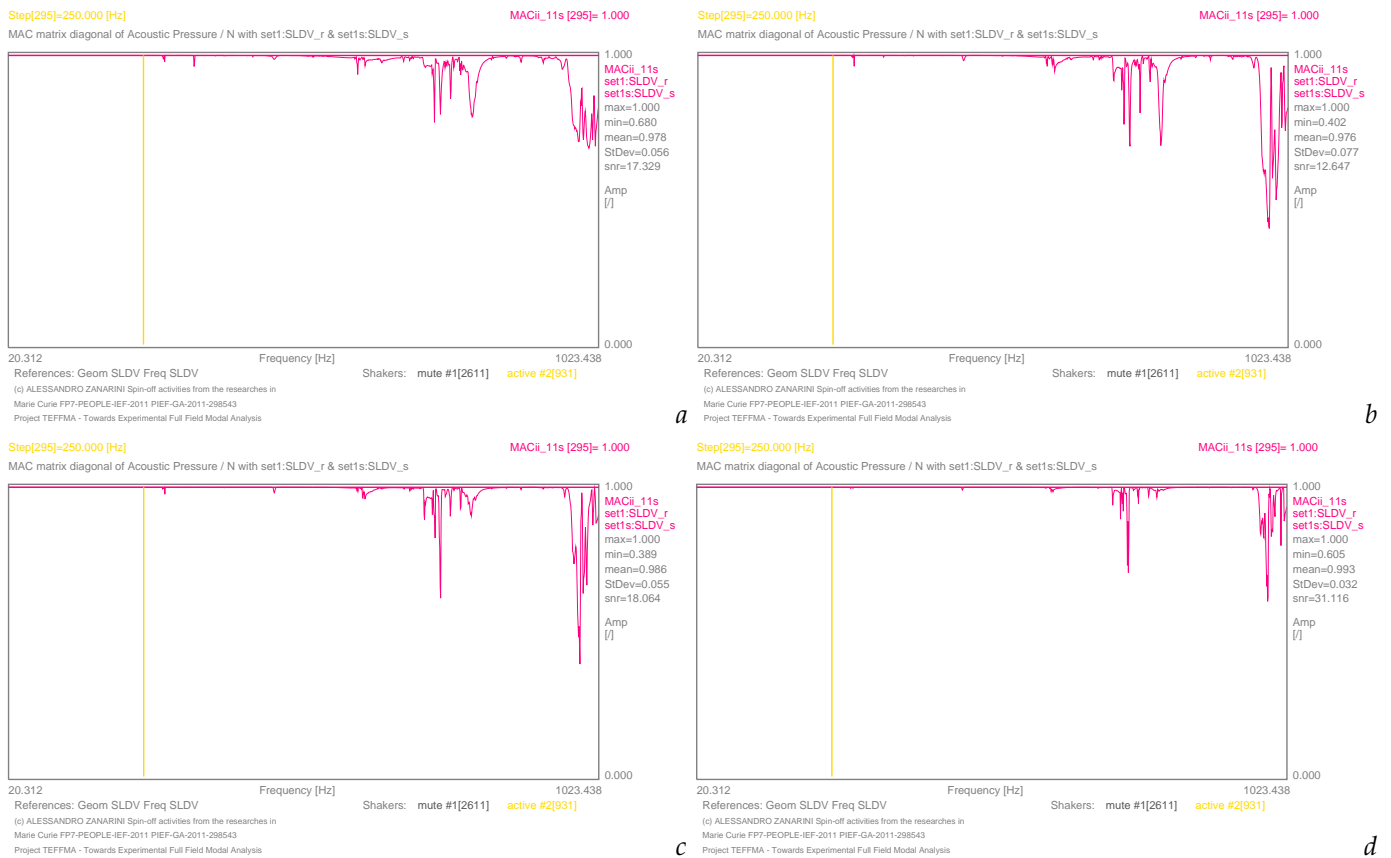


Figure 11. MACii graphs in the comparison of the *acoustic transfer matrix* as in Equations (14) and (18), at specific distances of 25 mm in (a), 75 mm in (b), 150 mm in (c), and 300 mm in (d) at the specific frequency of 250 Hz, with excitation from shaker 2.

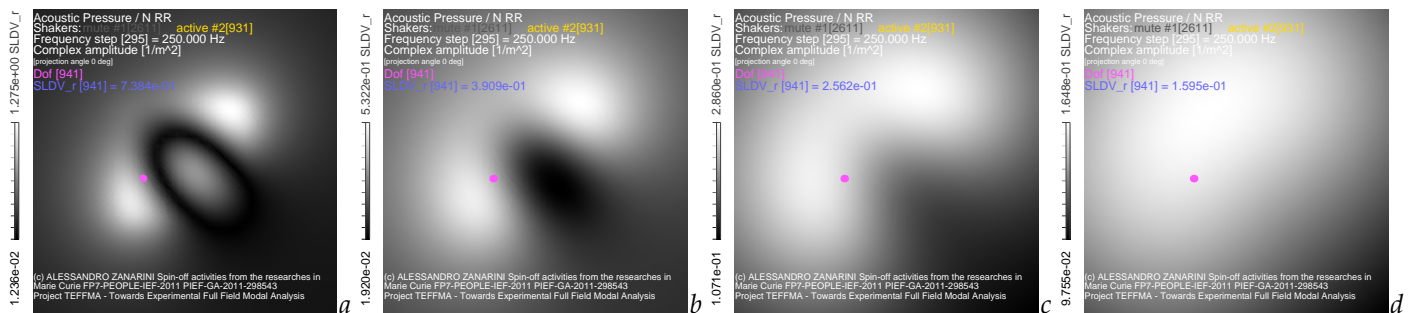


Figure 12. Vibro-acoustic FRF mapping of Equation (14) from *raw receptances* in Equation (1) at 250 Hz at specific distances of 25 mm in (a), of 75 mm in (b), of 150 mm in (c) and of 300 mm in (d) from shaker 2.

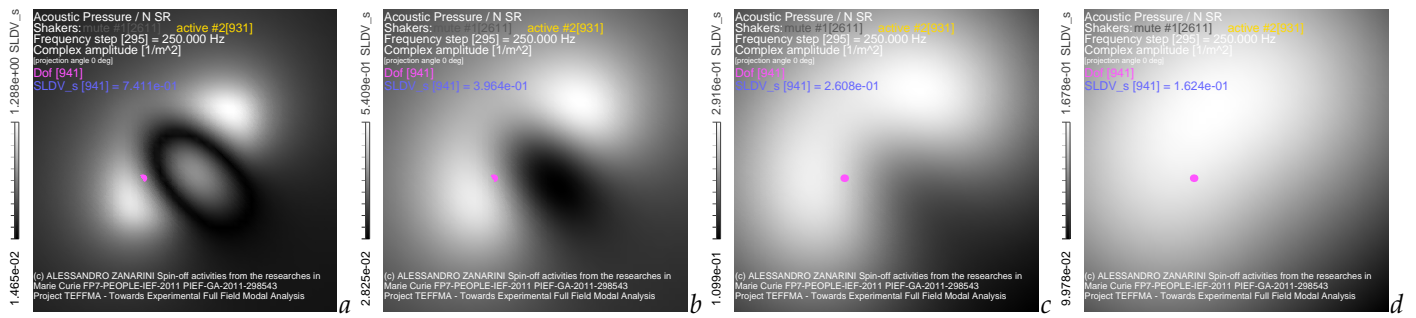


Figure 13. Vibro-acoustic FRF mapping of Equation (18) from *smoothed receptances* in Equation (2) at 250 Hz at specific distances of 25 mm in (a), of 75 mm in (b), of 150 mm in (c) and of 300 mm in (d) from shaker 2.

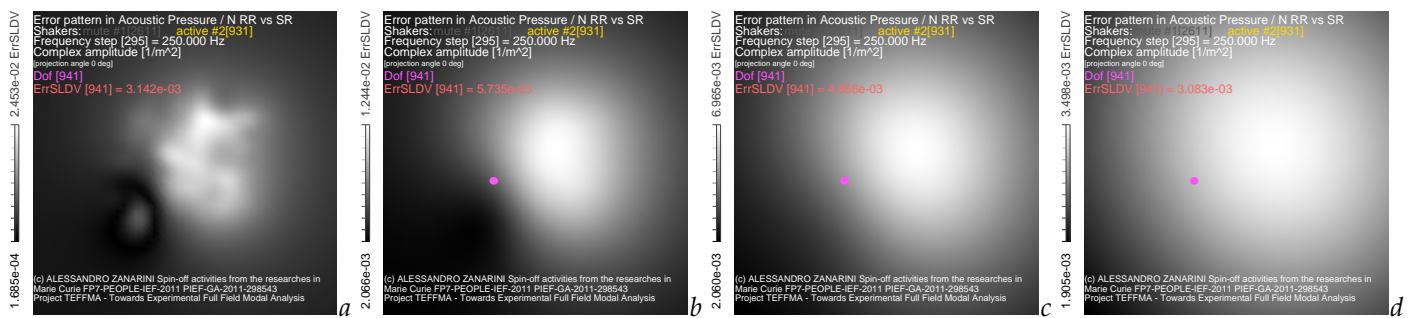


Figure 14. Error patterns of Equation (20) in vibro-acoustic FRF mapping from *experiment-based receptances* at 250 Hz at specific distances of 25 mm in (a), of 75 mm in (b), of 150 mm in (c) and of 300 mm in (d) from shaker 2.

Table 7. Ranges of complex amplitude [$1/m^2$] and the ratio of the extremes in the vibro-acoustic FRF fields—evaluated from the *raw receptances* in Equation (14), from the *smoothed receptances* in Equation (18)—and in the error function in Equation (20), at the specific frequency of 250 Hz.

Distance	Raw Max	Raw Min	Raw Ratio	Smooth Max	Smooth Min	Smooth Ratio	Err. Max	Err. Min	Err. Ratio
25 mm	1.275e+00	1.236e-02	103.16	1.288e+00	1.465e-02	87.92	2.453e-02	1.685e-04	145.58
75 mm	5.322e-01	1.920e-02	27.72	5.409e-01	2.825e-02	19.15	1.244e-02	2.066e-03	6.02
150 mm	2.860e-01	1.071e-01	2.67	2.916e-01	1.099e-01	2.65	6.965e-03	2.060e-03	3.38
300 mm	1.648e-01	9.755e-02	1.69	1.678e-01	9.978e-02	1.68	3.498e-03	1.905e-03	1.84

Table 8. Value of the complex amplitude [$1/m^2$] of the vibro-acoustic FRF field in acoustic dof 941 from the *raw receptances* in Equation (14), from the *smoothed receptances* in Equation (18), from the error function in Equation (20), and the ratio between the same error and the raw-based values at the specific frequency of 250 Hz.

Distance	Raw Value	Smoothed Value	Error Value	Ratio Error/Raw
25 mm	7.384e-01	7.411e-01	3.142e-03	4.255e-03
75 mm	3.909e-01	3.964e-01	5.735e-03	1.467e-02
150 mm	2.562e-01	2.608e-01	4.866e-03	1.899e-02
300 mm	1.595e-01	1.624e-01	3.083e-03	1.933e-02

3.3. Measurement-Related Noise Effects

As soon as the noise on the structural *receptance* field of Equation (1) is not any more evenly distributed, even if modulated in amplitude, new considerations have to

be made. During the measurement campaign of the TEFMA project [11–14], a specific measurement-system-related noise pattern was found. The specific instrumentation, more interesting for this theme, was that of SLDV, which provided characteristic sharp horizontal bands of highly manifest noise, superimposed to the structural dynamics of the plate. The equal distance among the bands might suggest some issues in the scanning mechanism, which were unknown during the acquisitions, the latter resulting from very good to optimal quality, according to the embedded software checks, as already stated in [14,34]. In Figures 15 and 20 examples are given at 284 Hz and 336 Hz, respectively. In both cases, the underneath ODS has a relatively low order of spatial complexity; therefore, the smoothing filter in Equation (2) can easily handle the task to isolate the measurement-related noise in Figures 15a and 20a for a clean undistorted shape, such as those in Figures 15b and 20b. The characteristic error pattern of Equation (3) can be seen in Figures 15c and 20c. Note that the example in Figure 20 has an uneven amplification of the noise amplitude, perhaps related to the deformation energy in the ODS; therefore, the *smoothed receptance* might have a larger distortion than that in Figure 15, as can be seen by comparing Figures 15c and 20c.

In Table 4, the fourth column presents slightly lower values than the third column only at the closer, or nearfield, distance of 25 mm, where the vibro-acoustic simulation is more influenced by the structural *receptance* shape; otherwise the difference is negligible, though at both frequencies (of 284 and 336 Hz) the MACii values are very close to unity, being in a flat region of the graphs, witnessing identifiability problems by the MACii function of Equation (22) for such type of measurement-related noise, as Figures 16 and 21 also show.

In Figure 17 the vibro-acoustic FRF field of Equation (14) is displayed in its complex amplitude at 284 Hz, as simulated starting from the *raw receptances*, at the four distances of interest. This time the resemblance of the *receptance map* of Equation (1) in Figure 15a appears less manifest to the vibro-acoustic FRF map, even at closer distances in Figure 17a, due to the specific and stronger measurement-related noise pattern; as expected, this low resemblance fades already in Figure 17b, but preserves a kind of triangular footprint. As the acoustic mesh is at 150 mm in Figure 17c, instead, the footprint of the *receptance map* fades into a more generic dome, whose curvature becomes even larger at the maximal distance of 300 mm in Figure 17d. Similar conclusions can also be drawn at 336 Hz for the Figure 22, obtained from the different shape of the *raw receptance* of Figure 20a, again with loss of the specific pattern in the acoustic mesh beginning at 150 mm away from the plate.

Figure 18a–d presents the vibro-acoustic simulations of Equation (18) evaluated from the *smoothed receptance map* of Equation (2) in Figure 15b at 284 Hz, with the same statements about the fading footprint of the *smoothed receptance map* as the distance increases. But now, with just a quick glance at Figure 17a–d, a difference in shape can be seen, due to the suppression of the specific measurement-related noise of Figure 15c from the pumping interface, particularly at closer distances of up to 75 mm in Figure 18a,b, where the footprint on the vibro-acoustic simulations is less sharp. Analogously, Figure 23a–d displays the vibro-acoustic simulations of Equation (18) evaluated from the *smoothed receptance map* of Equation (2) in Figure 20b and isolated noise pattern of Figure 20c at 336 Hz, again with a more articulated pattern of the vibro-acoustic maps from the *smoothed receptance map* till Figure 23b, but yet clearly different from the corresponding *raw receptance map*-related shapes in Figure 22a–d.

In order to quantify the differences between the *acoustic transfer function* maps in Figures 17 and 18, the corresponding error patterns in Equation (20) as the *complex-valued* difference between the vibro-acoustic FRF simulations at 284 Hz, obtained from the *raw* and *smoothed receptances*, are displayed in Figure 19. It appears clearly how the specific measurement-related noise on the *raw receptance map* of Figure 15a, isolated in Figure 15c, has an impact on the simulation, particularly the stronger band close to the structural dof 1 in the upper part of the picture, it having stronger velocities than the smoothed shape. At all the distances the error patterns of the *acoustic transfer matrix* in Figure 19a–d are now specific and related to the type of noise on the *receptance map*, even if a fading footprint can be seen with increasing distance of the acoustic mesh from the vibrating plate. The

same type of error patterns on the *acoustic transfer matrix* are extracted in Figure 24a–d at 336 Hz: this time the pictures are influenced more by the amplitude-modulating *receptances* of Figure 20, which locally amplify the measurement-related banded noise, as can be seen in the *receptance* noise pattern of Figure 20c, showing asymmetries in the error footprint at the lower distances of the vibro-acoustic simulations.

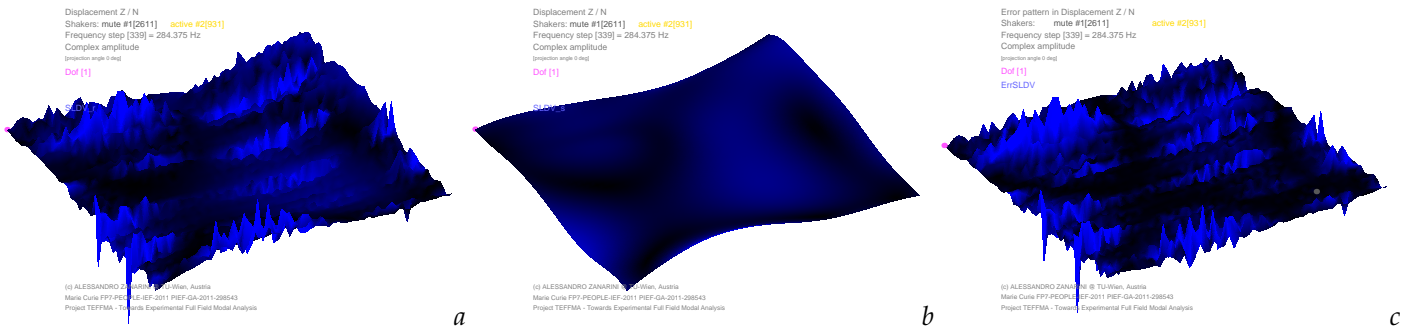


Figure 15. Examples of *receptance shapes* with their experiment-related noise (in (a), Equation (1)) against the smoothed version (in (b), Equation (2)) and related error pattern (in (c), Equation (3)) at the specific frequency of 284 Hz, with excitation from shaker 2.

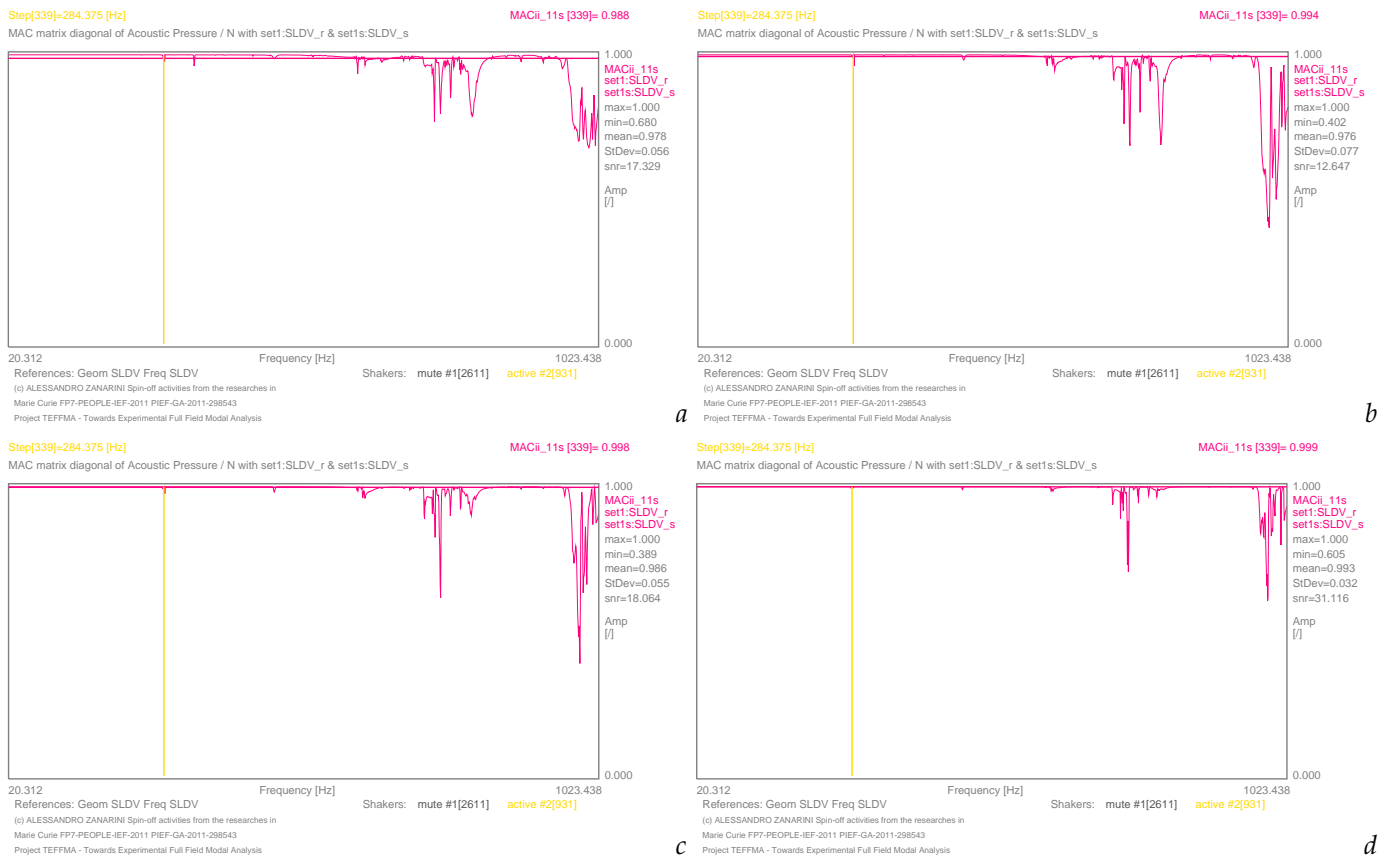


Figure 16. MACii graphs in the comparison of the *acoustic transfer matrix* as in Equations (14) and (18), at specific distances of 25 mm in (a), 75 mm in (b), 150 mm in (c), and 300 mm in (d) at the specific frequency of 284 Hz, with excitation from shaker 2.

Also Table 9 proposes the maximal values, the minimal values and their ratio of the vibro-acoustic FRF fields of Equations (14) and (18), coming from the *raw* and *smoothed receptances*, respectively, now at 284 Hz, together with the results of the error patterns of Equation (20). A bold difference can be seen in Table 9 compared to the similar Tables 5 and 7 in Section 3.2: for this type of measurement-related noise on the radiating source, it can be appreciated how at 284 Hz the *raw* and *smoothed receptance* dependant acoustic fields do not behave similarly; the vibro-acoustic error patterns are quite close in terms of ranges to those of the acoustic pressure over force in both the simulations, now with a much stronger (nearly 10×) ratio, fading with distance, but witness of a clear effect of the structural dynamics’ noise on the acoustic field. Instead, at 336 Hz, Table 11 describes a slightly different behaviour, with a milder ratio of the ranges, especially at lower distances for the acoustic error patterns, which are very close to the ratio of the *raw* and *smoothed receptance*-dependant fields. Note that all the ranges in Table 11 are much more closely spaced, in about the same magnitude, but with the acoustic error patterns in half the ranges of the other fields, therefore of relevance.

A punctual error evaluation in the complex amplitude of the vibro-acoustic FRF, together with the ratio between the acoustic error of Equation (20) and the simulation from *raw receptances* of Equation (14), can be run, as in Table 10 at 284 Hz or in Table 12 at 336 Hz, again in the acoustic mesh dof 941, previously mentioned. In Figure 3 the vibro-acoustic FRFs, obtained from the *raw* and *smoothed receptances*, are compared, showing a marginal error impact at 284 Hz and 75 mm of distance from the source (Figure 3b). Table 10 at 284 Hz states a more influenced vibro-acoustic behaviour, with higher noise effects, which means specifically that the acoustic error ratio slightly increases when passing from a distance of 25 mm to 75 mm from the vibrating plate, and then it fades slightly with further distancing, but it remains restrained in the range [0.059–0.094]. Instead, Table 12 at 336 Hz highlights much higher (roughly 10×) acoustic error ratios on the punctual function, but they remain quite constant as the distance is increased, in the range [0.659–0.706]. Therefore, the *receptances* of Figure 20 have a slightly stronger effect than those in Figure 15 in distorting the vibro-acoustic simulations, thanks to their amplitude modulation of the measurement-related noise.

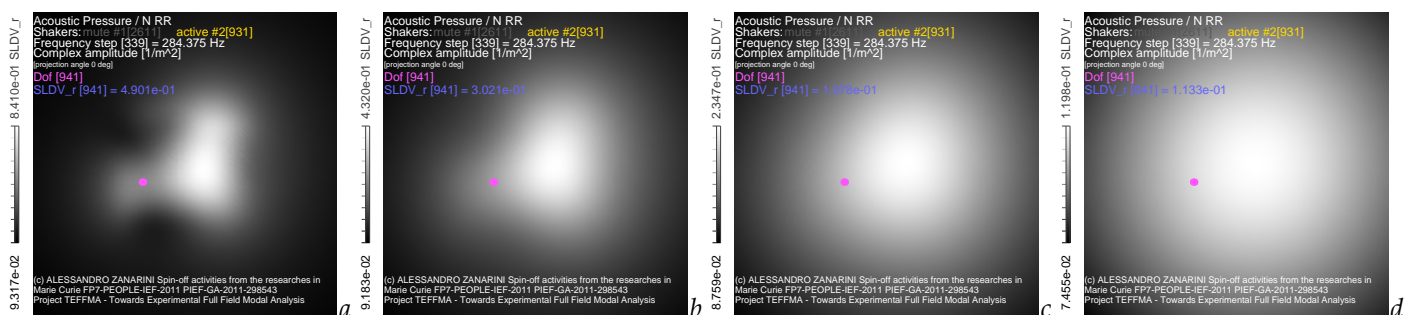


Figure 17. Vibro-acoustic FRF mapping of Equation (14) from *raw receptances* in Equation (1) at 284 Hz at specific distances of 25 mm in (a), of 75 mm in (b), of 150 mm in (c) and of 300 mm in (d) from shaker 2.

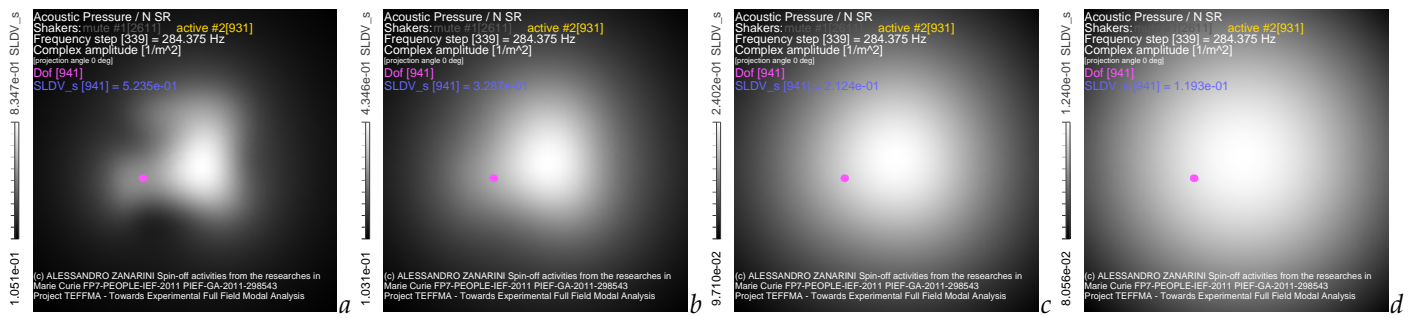


Figure 18. Vibro-acoustic FRF mapping of Equation (18) from *smoothed receptances* in Equation (2) at 284 Hz at specific distances of 25 mm in (a), of 75 mm in (b), of 150 mm in (c) and of 300 mm in (d) from shaker 2.

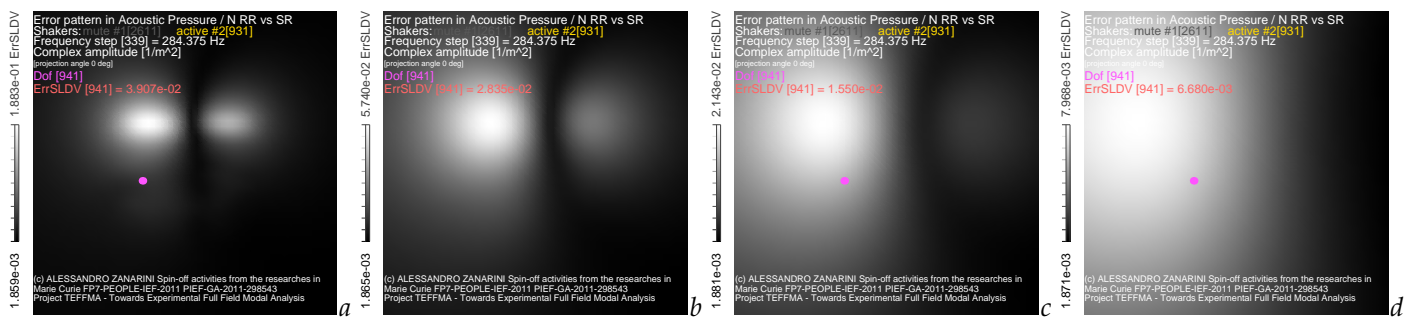


Figure 19. Error patterns of Equation (20) in vibro-acoustic FRF mapping from *experiment-based receptances* at 284 Hz at specific distances of 25 mm in (a), of 75 mm in (b), of 150 mm in (c) and of 300 mm in (d) from shaker 2.

Table 9. Ranges of complex amplitude [1/m²] and the ratio of the extremes in the vibro-acoustic FRF fields—evaluated from the *raw receptances* in Equation (14), from the *smoothed receptances* in Equation (18)—and in the error function in Equation (20), at the specific frequency of 284 Hz.

Distance	Raw Max	Raw Min	Raw Ratio	Smooth Max	Smooth Min	Smooth Ratio	Err. Max	Err. Min	Err. Ratio
25 mm	8.410e-01	9.317e-02	9.03	8.347e-01	1.051e-01	7.94	1.883e-01	1.859e-03	101.29
75 mm	4.320e-01	9.183e-02	4.70	4.346e-01	1.031e-01	4.22	5.740e-02	1.865e-03	30.78
150 mm	2.347e-01	8.759e-02	2.68	2.402e-01	9.710e-02	2.47	2.143e-02	1.881e-03	11.39
300 mm	1.198e-01	7.455e-02	1.61	1.240e-01	8.056e-02	1.54	7.968e-03	1.871e-03	4.26

Table 10. Value of the complex amplitude [1/m²] of the vibro-acoustic FRF field in acoustic dof 941 from the *raw receptances* in Equation (14), from the *smoothed receptances* in Equation (18), from the error function in Equation (20), and the ratio between the same error and the raw-based values at the specific frequency of 284 Hz.

Distance	Raw Value	Smoothed Value	Error Value	Ratio Error/Raw
25 mm	4.901e-01	5.235e-01	3.907e-02	7.972e-02
75 mm	3.021e-01	3.287e-01	2.835e-02	9.384e-02
150 mm	1.978e-01	2.124e-01	1.550e-02	7.836e-02
300 mm	1.133e-01	1.193e-01	6.680e-03	5.896e-02

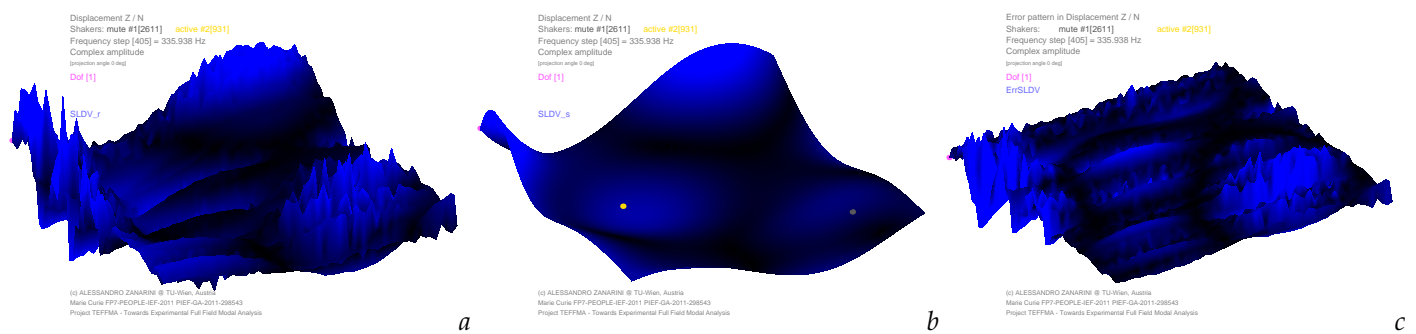


Figure 20. Examples of *receptance shapes* with their experiment-related noise (in (a), Equation (1)) against the smoothed version (in (b), Equation (2)) and related error pattern (in (c), Equation (3)) at the specific frequency of 336 Hz, with excitation from shaker 2.

3.4. Filtering-Related Noise Effects

The last type of distortion discussed here may come from an excessive correction of noise patterns by means of a spatial filter, whose tuning is directed towards a lower order complexity than is actually found on the *raw receptance* shape of Equation (1). The latter shape may exhibit intricate patterns, as the blending of a very complex structural dynamics, as well as of any type of modulated noises seen before, this being a uniformly distributed (see Section 3.2) or a measurement-related noise (see Section 3.3). The result is a cutting of all the higher spatial order complexities in the radiating shape, thus a distortion of the original shape and of the related elastic energy pattern, therefore having a strong repercussion on the velocity distribution that pumps energy into the acoustic domain.

In Figures 25 and 30 examples of excessive filtering on ODSs are given at 755 Hz and 991 Hz, respectively. In both cases, the underneath ODS has a relatively high order of spatial complexity; therefore, the smoothing filter, tuned for lower spatial complexity, badly handles the task to clean only the experiment noise in Figures 25a and 30a for a clean undistorted shape, giving instead over-smoothed and distorted shapes such as those in Figures 25b and 30b. Note that the example of Figure 25 has an uneven amplification of the measurement-related noise, with its bands of sharp amplitude and therefore higher spatial order complexity, compared to the underneath ODS. Once the *raw receptance* in Figure 25a is smoothed with a filter for a lower spatial complexity, the *smoothed receptance* in Figure 25b might have an even larger distortion than before, since not only the noise is cancelled, but also some of the structural dynamics' responses might have been cut or blended together (see in particular the double-dip bumps on the lower and right side of the shape, confirmed in the related error pattern of Figure 25c). Even more pronounced is the distortion at higher frequencies in Figure 30a–c: the central bump is drastically reduced to smooth the local spatial complexity in Figure 30a, similarly to what happens on the right side, where the newly *smoothed receptance* in Figure 30b has a quite different profile, with the high spatial frequency error pattern of Figure 30c, which is also amplitude-modulated by the ODS.

In Table 4, the fifth column (755 Hz) presents manifestly lower ([0.6–0.8]) MACii values than the first four columns at every distance (see also Figure 26); the sixth column (991 Hz) is even worse ([0.4–0.7], as in Figure 31), meaning that the distortions of the low spatial order filter are also easily detectable by the simple MACii functions of Equation (22). The impact at 755 Hz and at 991 Hz is much deeper at 75 mm and 150 mm away from the plate surface, whereas at 25 mm and 300 mm the impact is weaker and roughly comparable.

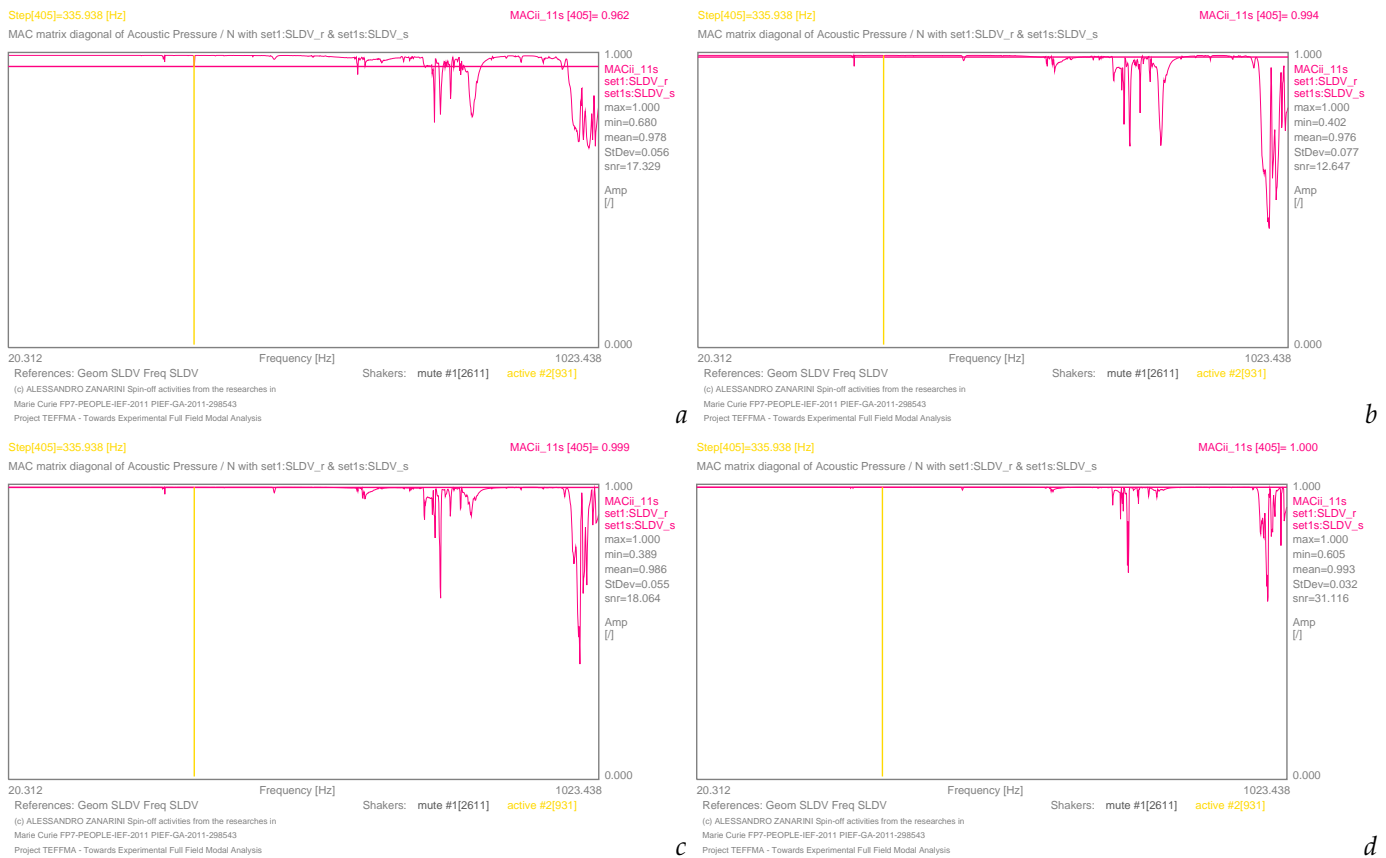


Figure 21. MACii graphs in the comparison of the *acoustic transfer matrix* as in Equations (14) and (18), at specific distances of 25 mm in (a), 75 mm in (b), 150 mm in (c), and 300 mm in (d) at the specific frequency of 336 Hz, with excitation from shaker 2.

In Figure 27a–d the vibro-acoustic FRF field is displayed in its complex amplitude at 755 Hz, as simulated starting from the *raw receptances*, at the four distances of interest. The resemblance of the *receptance map* of Equation (1) in Figure 25a appears clearly manifest to the vibro-acoustic FRF map of Equation (14), particularly at closer distances in Figure 27a, due to the measurement-related noise pattern of Equation (3), with a specific and stronger higher order of complexity and amplitude modulation. This resemblance fades, as expected with distance, in Figure 27b,c, but still preserves a kind of specific footprint. As the acoustic mesh is at 300 mm in Figure 27d, instead, the footprint of the *receptance map* fades into a more indistinct shape of large curvature. Similar conclusions can also be drawn at 991 Hz for Figure 32a–d, obtained from the different shape of the *raw receptance* of Figure 30a, again with a loss of the distinctive ridge pattern from 150 mm away from the plate as in Figure 32c, but still different from a regular dome also at 300 mm as in Figure 32d.

Figure 28 presents the vibro-acoustic simulations of Equation (18) evaluated from the *smoothed receptance map* of Equation (2) in Figure 25b at 755 Hz, with the same statements about the fading footprint of the *smoothed receptance map* as the distance increases. It is clear now how a difference in shapes can be seen from the corresponding pictures in Figure 27, due to the suppression from the pumping interface, by means of the lower spatial order filter, of the specific measurement-related noise isolated in Figure 25c, modulated in amplitude by the ODS. This difference can be appreciated particularly at closer distances up to 75 mm in Figure 28a,b, from which the footprint starts to be less defined. Similarly, due to the error in Figure 30c, Figure 33 displays the vibro-acoustic simulations evaluated from the *smoothed receptance map* of Figure 30b at 991 Hz, again with a more articulated pattern till Figure 33b, but sufficiently different from the corresponding ones in Figure 32.

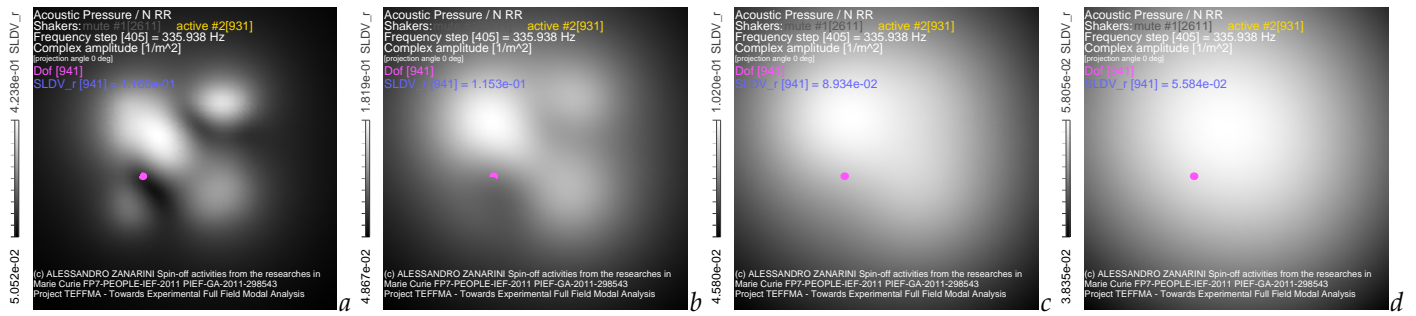


Figure 22. Vibro-acoustic FRF mapping of Equation (14) from raw receptances in Equation (1) at 336 Hz at specific distances of 25 mm in (a), of 75 mm in (b), of 150 mm in (c) and of 300 mm in (d) from shaker 2.

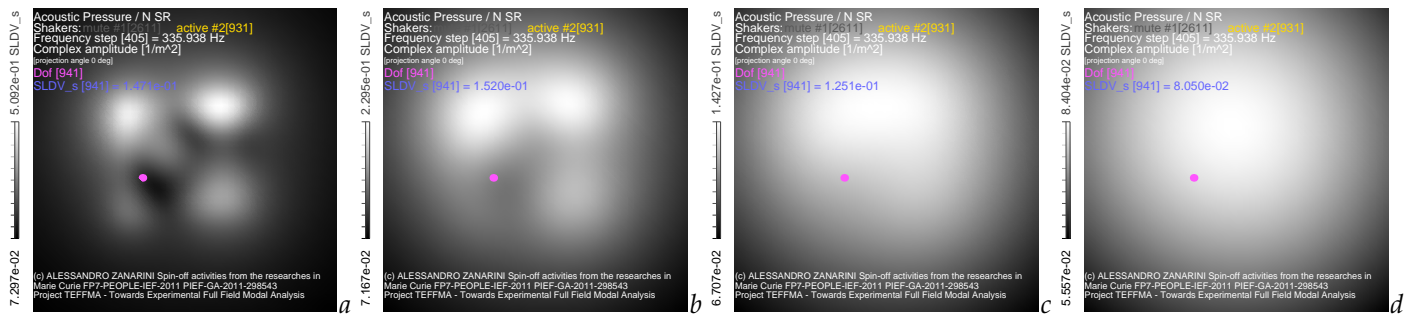


Figure 23. Vibro-acoustic FRF mapping of Equation (18) from smoothed receptances in Equation (2) at 336 Hz at specific distances of 25 mm in (a), of 75 mm in (b), of 150 mm in (c) and of 300 mm in (d) from shaker 2.

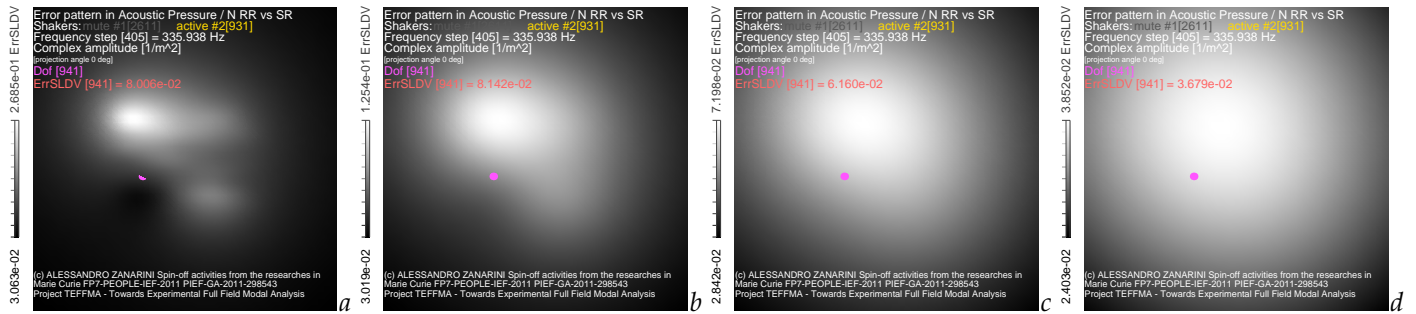


Figure 24. Error patterns of Equation (20) in vibro-acoustic FRF mapping from experiment-based receptances at 336 Hz at specific distances of 25 mm in (a), of 75 mm in (b), of 150 mm in (c) and of 300 mm in (d) from shaker 2.

Table 11. Ranges of complex amplitude [$1/m^2$] and the ratio of the extremes in the vibro-acoustic FRF fields—evaluated from the raw receptances in Equation (14), from the smoothed receptances in Equation (18)—and in the error function in Equation (20), at the specific frequency of 336 Hz.

Distance	Raw Max	Raw Min	Raw Ratio	Smooth Max	Smooth Min	Smooth Ratio	Err. Max	Err. Min	Err. Ratio
25 mm	4.238e-01	5.052e-02	8.39	5.092e-01	7.297e-02	6.98	2.685e-01	3.063e-02	8.77
75 mm	1.819e-01	4.867e-02	3.74	2.295e-01	7.167e-02	3.20	1.254e-01	3.019e-02	4.15
150 mm	1.020e-01	4.580e-02	2.23	1.427e-01	6.707e-02	2.13	7.198e-02	2.842e-02	2.53
300 mm	5.805e-02	3.835e-02	1.51	8.404e-02	5.557e-02	1.51	3.852e-02	2.403e-02	1.60

Table 12. Value of the complex amplitude [$1/m^2$] of the vibro-acoustic FRF field in acoustic dof 941 from the *raw receptances* in Equation (14), from the *smoothed receptances* in Equation (18), from the error function in Equation (20), and the ratio between the same error and the raw-based values at the specific frequency of 336 Hz.

Distance	Raw Value	Smoothed Value	Error Value	Ratio Error/Raw
25 mm	1.166e-01	1.471e-01	8.006e-02	6.866e-01
75 mm	1.153e-01	1.520e-01	8.142e-02	7.062e-01
150 mm	8.934e-02	1.251e-01	6.160e-02	6.895e-01
300 mm	5.584e-02	8.050e-02	3.679e-02	6.588e-01

In order to quantify the differences between the *acoustic transfer function* maps of Equations (14) and (18) in Figures 27 and 28, the corresponding error patterns in Equation (20) at 755 Hz are displayed in Figure 29a–d. It appears clearly how the suppression of higher order complexities and specific measurement-related noise, on the *raw receptance map* of Figure 25a and isolated in Figure 25c, has an impact on the simulation, particularly from the dual bands emphasised on the left side by the ODS amplitude, having stronger radiation power than the *smoothed* shape. At all the distances the acoustic error patterns in Figure 29 are now related to the distortion of the ODS, particularly close to the magenta acoustic dof 941 but also on lower bumps, even if a fading footprint can be seen with increasing distance of the acoustic mesh from the vibrating plate. The same type of acoustic error patterns of Equation (20) are extracted in Figure 34a–d at 991 Hz: the pictures appear heavily influenced by the filter-related distortions on the *receptance map* of Figure 30a, and isolated in Figure 30c with local amplification of the measurement-related banded noise, showing a marked L-shaped footprint around dof 941, especially at the lower distances of the vibro-acoustic simulations as in Figure 34a,b, clearly recalling the ridge of Figure 4a,b.

Table 13 continues the analysis on the maximal values, the minimal values and their ratio, now at 755 Hz, of the vibro-acoustic FRF fields in Equations (14), (18) and (20), coming from the *raw* and *smoothed receptances* of Equations (1) and (2), together with those of the acoustic error patterns of the vibro-acoustic simulations. A remarkable difference can be seen compared to the similar Tables 5 and 7 in Section 3.2, or Tables 9 and 11 in Section 3.3: for this type of filtering-related noise on the radiating source, it can be appreciated how at 755 Hz the *raw* and *smoothed receptance* dependant *acoustic transfer function* fields do behave very differently at any distance, in terms of ranges and their ratio. Furthermore, the vibro-acoustic error patterns are in the same ranges of the vibro-acoustic FRFs in the *raw receptance* based simulations, but with a much restrained ratio of ranges, fading with distance, but witness of a clear effect of distortion on the acoustic field. Furthermore, at 991 Hz, Table 15 describes an even more extreme behaviour, with a huge ratio of the ranges for the *raw receptance* based simulation, especially at lower distances, but much greater than seen before at far distances as well. On the other side, the *smoothed receptance* based simulations have strongly restrained ratios of ranges, suggesting clearly a very clean, then distorted, field from that coming from the *raw receptance*. Simultaneously, the ranges for the acoustic error patterns can be seen to be very close to those of the *raw* and *smoothed receptance* dependant fields, but in particular to be too similar in magnitude to the *smoothed receptance* based simulations, as another hint of great distortion due to excessive filtering.

A punctual error evaluation in the complex amplitude of the vibro-acoustic FRFs, together with the ratio between the acoustic error of Equation (20) and the simulation from *raw receptances* of Equation (14), can also be run in Table 14 at 755 Hz or in Table 16 at 991 Hz, again in the acoustic mesh dof 941. In Figure 3 the vibro-acoustic FRFs of Equations (14) and (18), obtained from the *raw* and *smoothed receptances* in Equations (1) and (2), are compared, showing a heavy error impact at 755 Hz and 150 mm of distance from the source (Figure 3c), in terms of complex amplitude, and even more so in terms of phase. At 911 Hz and 300 mm (Figure 3d), the difference of the complex amplitude

between *raw* and *smoothed receptances* based simulations is even greater, whereas the phase difference is more constrained. Table 14 at 755 Hz states a boldly influenced vibro-acoustic behaviour, with noise effects of the same magnitude as the function values; furthermore, the error ratio strongly increases (roughly 3×) when passing from a distance of 25 mm to 75 mm from the vibrating plate, and then it grows further with greater distancing, resulting restrained in the range of [0.634–2.674]. Table 16 at 991 Hz highlights even higher error ratios on the punctual function, with a steep increase as the distance grows, in the huge range of [0.560–4.788]. It can be stated that low-order complexity filtering on the *receptances* of Figures 25 and 30 has a heavy effect in distorting the vibro-acoustic simulations, due to the suppression of energy in the amplitude modulation of the measurement-related noise, but also in the structural dynamics’ responses.

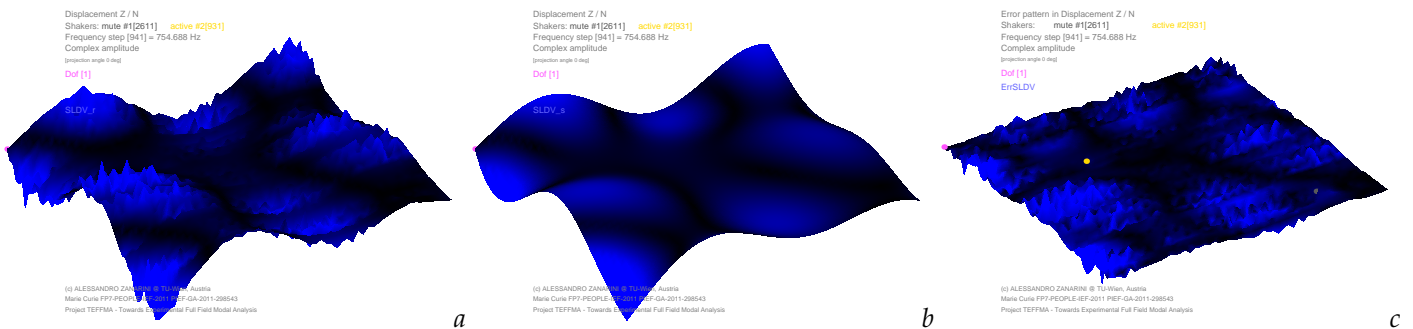


Figure 25. Examples of *receptance shapes* with their experiment-related noise (in (a), Equation (1)) against the smoothed version (in (b), Equation (2)) and related error pattern (in (c), Equation (3)) at the specific frequency of 755 Hz, with excitation from shaker 2.

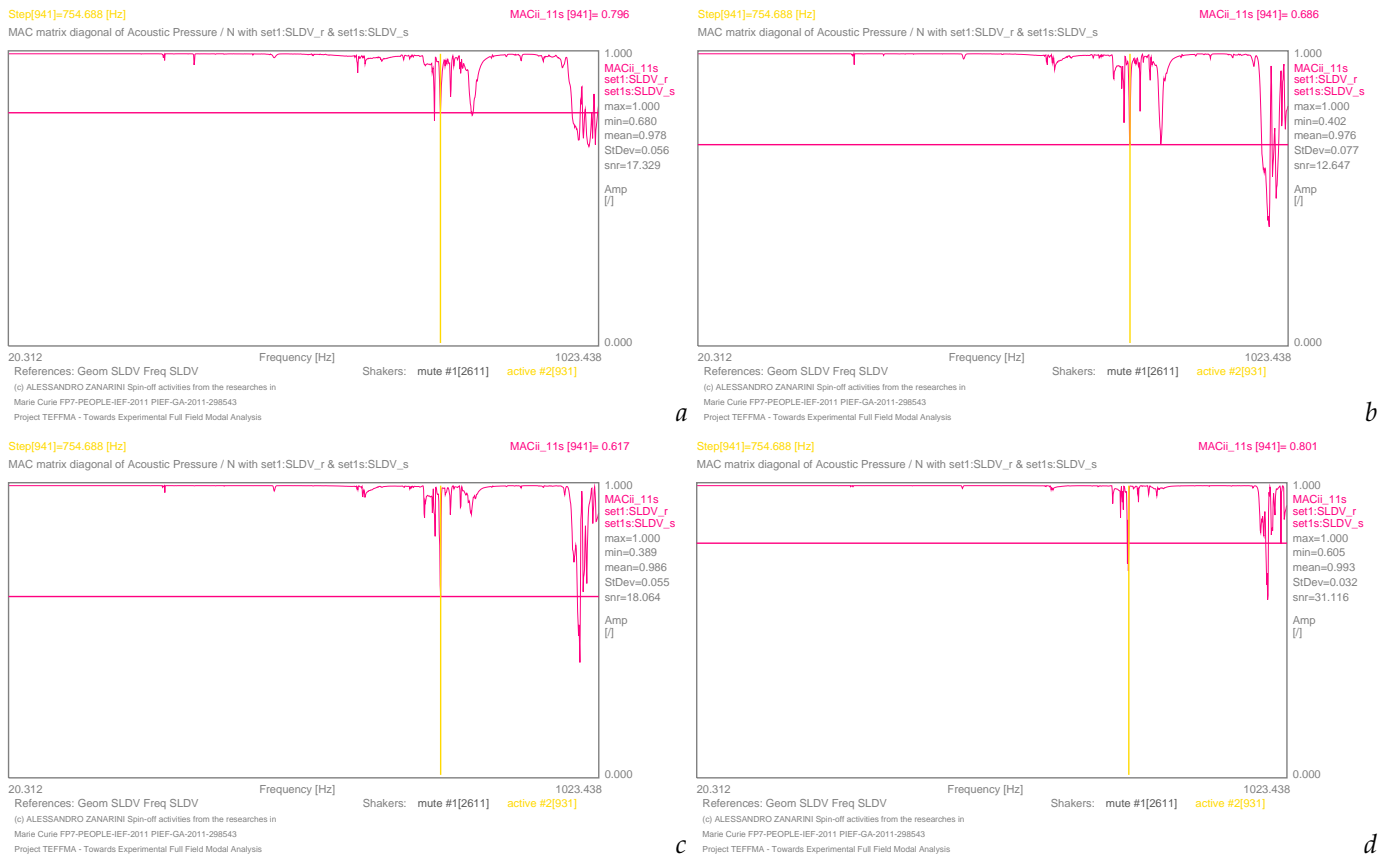


Figure 26. MACii graphs in the comparison of the *acoustic transfer matrix* as in Equations (14) and (18), at specific distances of 25 mm in (a), 75 mm in (b), 150 mm in (c), and 300 mm in (d) at the specific frequency of 755 Hz, with excitation from shaker 2.

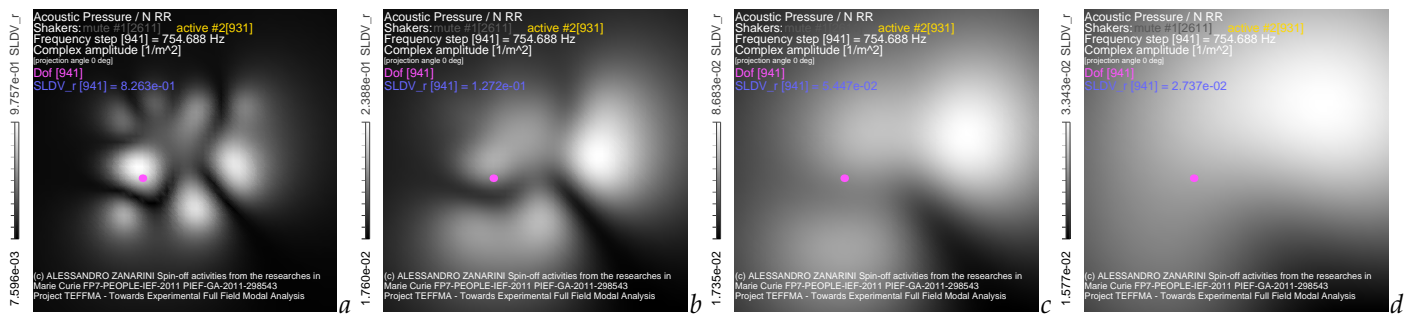


Figure 27. Vibro-acoustic FRF mapping of Equation (14) from *raw receptances* in Equation (1) at 755 Hz at specific distances of 25 mm in (a), of 75 mm in (b), of 150 mm in (c) and of 300 mm in (d) from shaker 2.

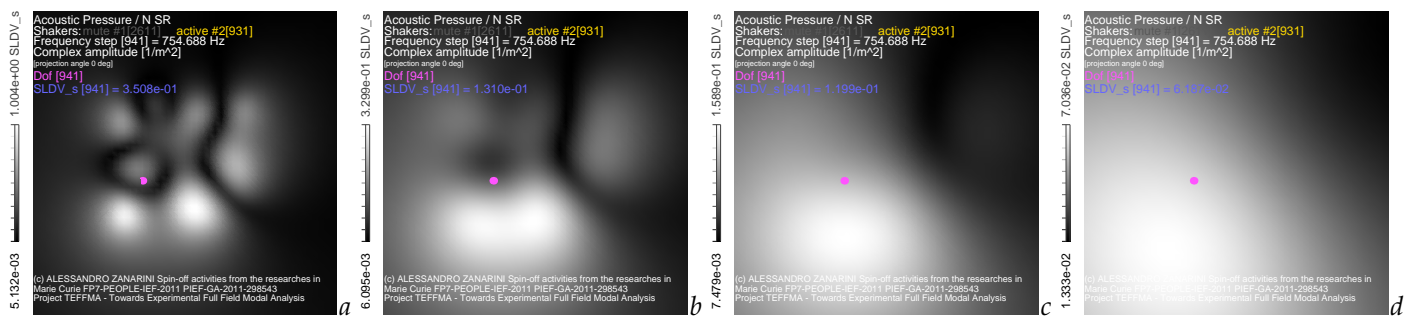


Figure 28. Vibro-acoustic FRF mapping of Equation (18) from *smoothed receptances* in Equation (2) at 755 Hz at specific distances of 25 mm in (a), of 75 mm in (b), of 150 mm in (c) and of 300 mm in (d) from shaker 2.

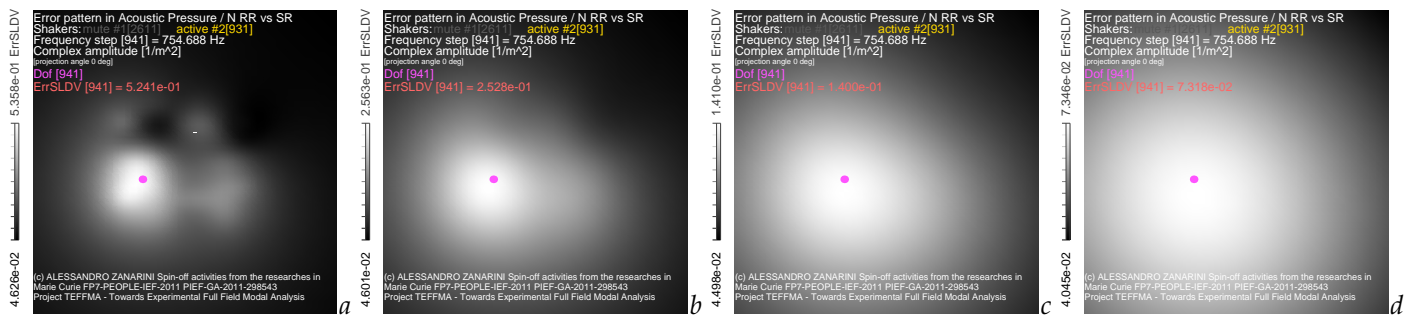


Figure 29. Error patterns of Equation (20) in vibro-acoustic FRF mapping from *experiment-based receptances* at 755 Hz at specific distances of 25 mm in (a), of 75 mm in (b), of 150 mm in (c) and of 300 mm in (d) from shaker 2.

Table 13. Ranges of complex amplitude [$1/m^2$] and the ratio of the extremes in the vibro-acoustic FRF fields—evaluated from the *raw receptances* in Equation (14), from the *smoothed receptances* in Equation (18)—and in the error function in Equation (20), at the specific frequency of 755 Hz.

Distance	Raw Max	Raw Min	Raw Ratio	Smooth Max	Smooth Min	Smooth Ratio	Err. Max	Err. Min	Err. Ratio
25 mm	9.757e-01	7.596e-03	128.45	1.004e+00	5.132e-03	195.64	5.358e-01	4.626e-02	11.58
75 mm	2.388e-01	1.760e-02	13.57	3.299e-01	6.095e-03	54.13	2.563e-01	4.601e-02	5.57
150 mm	8.683e-02	1.735e-02	5.00	1.589e-01	7.479e-03	21.25	1.410e-01	4.498e-02	3.13
300 mm	3.343e-02	1.577e-02	2.12	7.036e-02	1.333e-02	5.28	7.346e-02	4.045e-02	1.82

Table 14. Value of the complex amplitude [$1/\text{m}^2$] of the vibro-acoustic FRF field in acoustic dof 941 from the *raw receptances* in Equation (14), from the *smoothed receptances* in Equation (18), from the error function in Equation (20), and the ratio between the same error and the raw-based values at the specific frequency of 755 Hz.

Distance	Raw Value	Smoothed Value	Error Value	Ratio Error/Raw
25 mm	8.263e-01	3.508e-01	5.241e-01	6.343e-01
75 mm	1.272e-01	1.310e-01	2.528e-01	1.987e+00
150 mm	5.447e-02	1.199e-01	1.400e-01	2.559e+00
300 mm	2.737e-02	6.187e-02	7.318e-02	2.674e+00

4. Discussion

The purpose of this article is to discuss how the noise measured on the structural dynamics can influence the vibro-acoustic FRF simulations. In Section 3 examples of the whole *acoustic transfer matrix* $V_{aq}(\omega)$ from Section 2.3 were shown over the entire acoustic mesh at specific frequencies and distances, when shaker 2 was used; in particular, in Sections 3.2–3.4, three different types of noise patterns were highlighted over the structural *receptances* from real testing. The frequencies were selected on the whole broad frequency band, therefore also outside the resonances, as presenting specific behaviours, which may enter into the acoustic responses when the structure is excited with a broad signature. Furthermore, they may leave traces in the modal identification [13,32]. These results were precisely discussed by means of the quantitative tools proposed in Section 2.4. Note again how the vibro-acoustic simulations retained the real-life, unsimplified, *complex-valued* relations and phase delays, coming from the underneath *complex-valued receptance* matrix in Equation (1), obtained directly from the experiments of Section 2.1, but blended in the *complex-valued* summation in $V_{aq}(\omega)$ of Equation (14), without any artificial noise model nor regularisation.

Table 17 summarises the ratio between the evaluated vibro-acoustic error against the raw vibro-acoustic transfer function value in acoustic dof 941; each pair of columns (first-second, third-fourth, fifth-sixth) is related to each type of error in the *receptance* source as discussed in Section 3. This ratio goes from a negligible to a strong relevance of noise issues in the vibro-acoustic simulations, showing when the smoothed results can clearly be distorted in comparison with those obtainable from the raw experiments. After the development of such a quantitative comparison of datasets, run at four distances from nearfield to medium distance, it can be easily stated that only a uniformly distributed random noise on experimental structural *raw receptances* has a very limited impact on vibro-acoustic FRF simulations, at close distance from the vibrating plate. However, it is sufficient that an ODS modulates—in the spatial domain—the amplitude of the scattered noise, to start noticing some divergence in the results, as commented on Section 3.2. Once the noise on the experimental structural *raw receptances* has specific patterns, such as those related to a specific measurement system, also modulated by the ODS pattern, the assumption of uniform distribution in the noise is lost, and clear effects were commented on Section 3.3. The stronger distortions—here documented in Section 3.4—originated from the excessive filtering of experimental datasets, by means of a filter with a lower spatial complexity than that found on the experimental structural *raw receptances* and real noise distributions (e.g., the specific measurement-related noise, modulated in amplitude and phase by the *complex-valued* ODS). This latter problem suggests the usage in future research of a smoothing filter with adaptive spatial order to the complexity of the specific structural dynamics and real-life noise patterns.

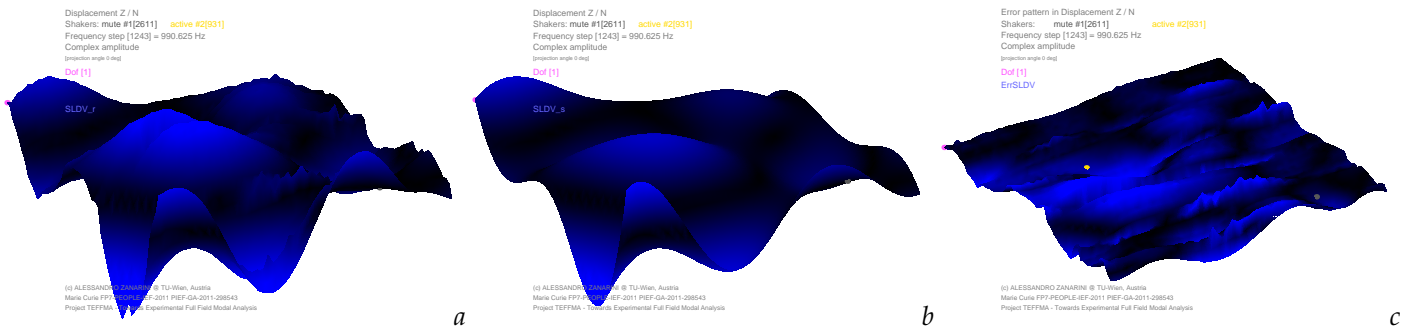


Figure 30. Examples of *receptance shapes* with their experiment-related noise (in (a), Equation (1)) against the smoothed version (in (b), Equation (2)) and related error pattern (in (c), Equation (3)) at the specific frequency of 991 Hz, with excitation from shaker 2.

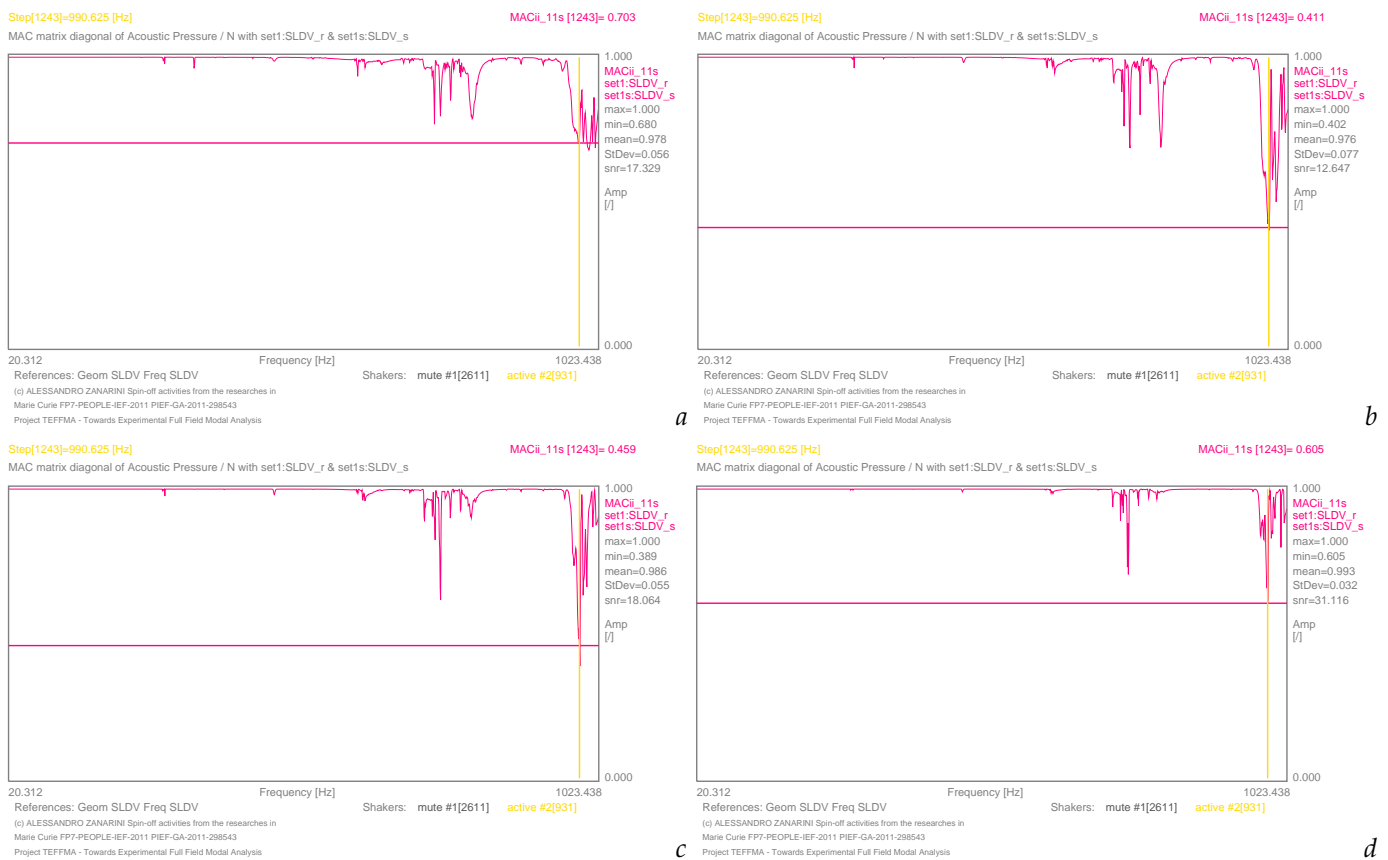


Figure 31. MACii graphs in the comparison of the *acoustic transfer matrix* as in Equations (14) and (18), at specific distances of 25 mm in (a), 75 mm in (b), 150 mm in (c), and 300 mm in (d) at the specific frequency of 991 Hz, with excitation from shaker 2.

5. Conclusions

By exploiting the possibilities in vibro-acoustics emerging from *experiment-based full-field tools*, specifically the *optical full-field measurements*, the effects of three different types of errors in the raw structural measurements were highlighted regarding vibro-acoustic FRF simulations on a dense mesh of acoustic dofs, going beyond the common assumption of the uniform distribution of structural noise with residual acoustic radiation effects.

The unprecedented mapping ability, in both spatial and frequency domains, permitted novel analyses of real-life noise impacts in vibro-acoustic prediction paradigms, where the real-life structural dynamics of the radiating surface is entirely retained in the acoustic simulation with great accuracy, but without assumptions on the materials’ dynamic behaviour,

nor on unknown boundary conditions; no residual error was inherited from any identification nor structural model updating of the vibrating source, for a clear advancement of vibro-acoustic experimental benchmarks in the design procedures of complex structures.

Further experiments in the acoustic domain, to verify these noise effect predictions on sound radiation, might be needed in the future to give assurance of the achieved results, for an increased awareness of full-field optical measurements' capabilities for the most demanding NVH predictions in coupled domains, like in fluid-structure interactions.

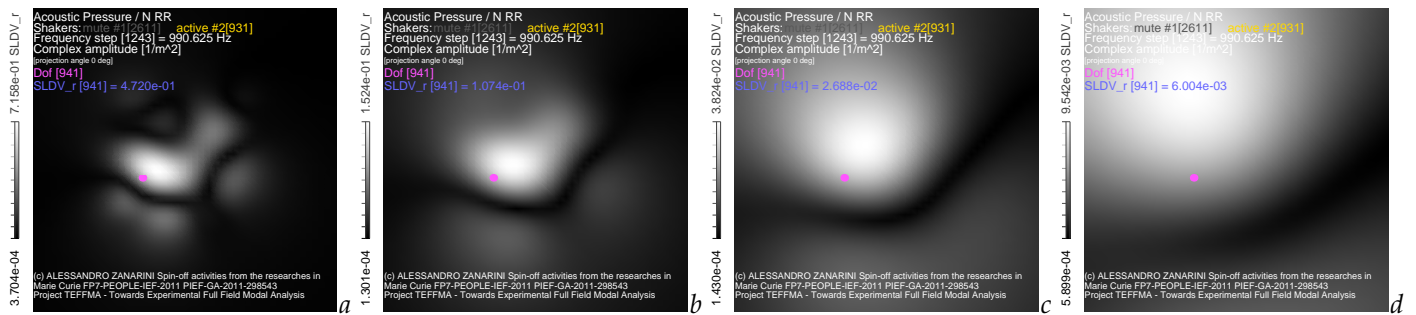


Figure 32. Vibro-acoustic FRF mapping of Equation (14) from *raw receptances* in Equation (1) at 991 Hz at specific distances of 25 mm in (a), of 75 mm in (b), of 150 mm in (c) and of 300 mm in (d) from shaker 2.

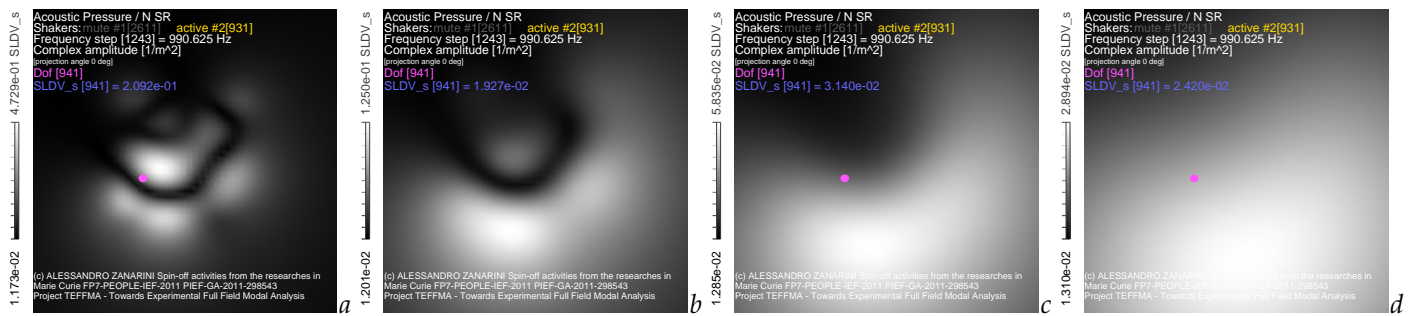


Figure 33. Vibro-acoustic FRF mapping of Equation (18) from *smoothed receptances* in Equation (2) at 991 Hz at specific distances of 25 mm in (a), of 75 mm in (b), of 150 mm in (c) and of 300 mm in (d) from shaker 2.

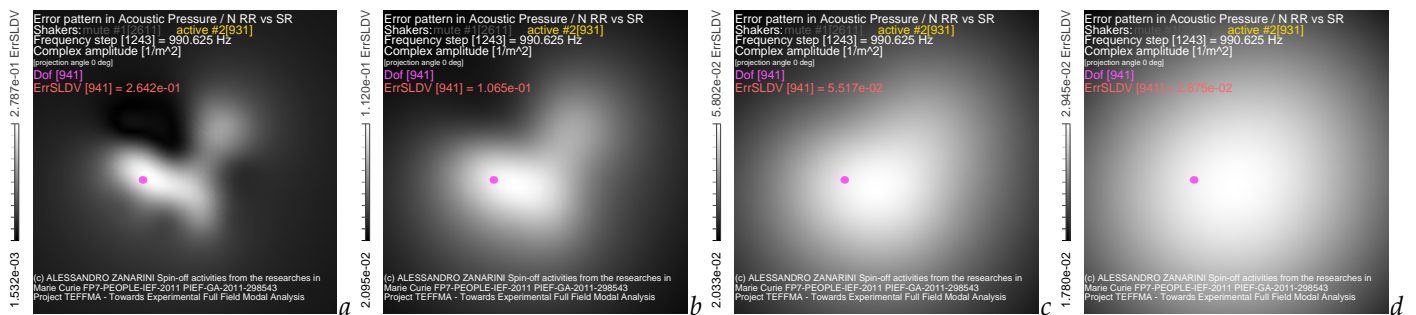


Figure 34. Error patterns of Equation (20) in vibro-acoustic FRF mapping from *experiment-based receptances* at 991 Hz at specific distances of 25 mm in (a), of 75 mm in (b), of 150 mm in (c) and of 300 mm in (d) from shaker 2.

Table 15. Ranges of complex amplitude [$1/m^2$] and the ratio of the extremes in the vibro-acoustic FRF fields—evaluated from the *raw receptances* in Equation (14), from the *smoothed receptances* in Equation (18)—and in the error function in Equation (20), at the specific frequency of 991 Hz.

Distance	Raw Max	Raw Min	Raw Ratio	Smooth Max	Smooth Min	Smooth Ratio	Err. Max	Err. Min	Err. Ratio
25 mm	7.158e-01	3.704e-04	1932.51	4.729e-01	1.173e-02	40.32	2.787e-01	1.532e-03	181.91
75 mm	1.524e-01	1.301e-04	1171.41	1.250e-01	1.201e-02	10.41	1.120e-01	2.095e-02	5.35
150 mm	3.824e-02	1.430e-04	267.41	5.835e-02	1.285e-02	4.54	5.802e-02	2.033e-02	2.85
300 mm	9.542e-03	5.899e-04	16.18	2.894e-02	1.310e-02	2.21	2.945e-02	1.780e-02	1.65

Table 16. Value of the complex amplitude [$1/m^2$] of the vibro-acoustic FRF field in acoustic dof 941 from the *raw receptances* in Equation (14), from the *smoothed receptances* in Equation (18), from the error function in Equation (20), and the ratio between the same error and the raw-based values at the specific frequency of 991 Hz.

Distance	Raw Value	Smoothed Value	Error Value	Ratio Error/Raw
25 mm	4.720e-01	2.092e-01	2.642e-01	5.597e-01
75 mm	1.074e-01	1.927e-02	1.065e-01	9.916e-01
150 mm	2.688e-02	3.140e-02	5.517e-02	2.052e+00
300 mm	6.004e-03	2.420e-02	2.875e-02	4.788e+00

Table 17. Ratio between the evaluated error against the raw function value in acoustic dof 941, at specific frequencies of the comparison between vibro-acoustic maps, obtained from raw and smoothed optical full-field *receptances*, as in the last column of Tables 6, 8, 10, 12, 14 and 16.

Distance	127 Hz	250 Hz	284 Hz	336 Hz	755 Hz	991 Hz
25 mm	5.866e-03	4.255e-03	7.972e-02	6.866e-01	6.343e-01	5.597e-01
75 mm	7.818e-03	1.467e-02	9.384e-02	7.062e-01	1.987e+00	9.916e-01
150 mm	9.758e-03	1.899e-02	5.896e-02	6.895e-01	2.559e+00	2.052e+00
300 mm	1.068e-02	1.933e-02	5.896e-02	6.588e-01	2.674e+00	4.788e+00

Funding: TEFMA project ended in 2015; no further specific funding was received afterwards.

Data Availability Statement: Not applicable.

Acknowledgments: This activity is a spin-off of the Project TEFMA (Towards Experimental Full Field Modal Analysis), funded by the European Commission at the Technische Universitaet Wien, through the Marie Curie FP7-PEOPLE-IEF-2011 PIEF-GA-2011-298543 grant, for which the Research Executive Agency is greatly acknowledged. TU-Wien, in the person of Johann Wassermann and his staff, are kindly acknowledged for having hosted the TEFMA project of the author at the *Schwingungs-und Strukturanalyse/Optical Vibration Measurement Laboratory*. The workstation used to extensively process the datasets and code the acoustic radiation was provided by the author on his own savings. Professor Roberta Mullini is wholeheartedly acknowledged for her care in the English proofreading of the text.

Conflicts of Interest: The author declares no conflict of interest.

Abbreviations

The following abbreviations are used in this manuscript:

DIC	Digital image correlation
dof	Degree of freedom
EFFMA	Experimental full-field modal analysis

EMA	Experimental modal analysis
ESPI	Electronic speckle pattern interferometry
FRAC	Frequency response assurance criterion
FRF	Frequency response function
MAC	Modal assurance criterion
NDT	Non-destructive testing
NVH	Noise and vibration harshness
ODS	Operative deflection shape
SLDV	Scanning laser Doppler vibrometer
(ω)	Frequency dependency
$X(\omega)$	Displacement map
$F(\omega)$	Excitation force
$H_d(\omega)$	Receptance map
<i>men</i>	$m \times 10^n$ in C-language scientific/engineering notation, with <i>m</i> mantissa and <i>n</i> exponent

References

- Kirkup, S. Computational solution of the acoustic field surrounding a baffled panel by the Rayleigh integral method. *Appl. Math. Model.* **1994**, *18*, 403–407. [CrossRef]
- Gérard, F.; Tournour, M.; Masri, N.; Cremers, L.; Felice, M.; Selmane, A. Acoustic transfer vectors for numerical modeling of engine noise. *Sound Vib.* **2002**, *36*, 20–25.
- Citarella, R.; Federico, L.; Cicatiello, A. Modal acoustic transfer vector approach in a FEM–BEM vibro-acoustic analysis. *Eng. Anal. Bound. Elem.* **2007**, *31*, 248–258. [CrossRef]
- Desmet, W. *Boundary Element Method in Acoustics*; Technical Report; Noise & Vibration Research Group, Mechanical Engineering Department, Katholieke Universiteit Leuven: Leuven, Belgium, 2004; In ISAAC 15, Course on Numerical and Applied Acoustics, Katholieke Universiteit Leuven, Belgium, Mechanical Engineering Department, Noise & Vibration Research Group . Available online: <https://www.isma-isaac.be> (accessed on 23 April 2023).
- Fahy, F. *Foundations of Engineering Acoustics*; Academic Press: London, UK, 2003; pp. 1–443. [CrossRef]
- Kirkup, S.; Thompson, A. Computing the Acoustic Field of a Radiating Cavity by the Boundary Element—Rayleigh Integral Method (BERIM). In Proceedings of the World Congress on Engineering, WCE 2007, London, UK, 2–4 July 2007; Ao, S.I., Gelman, L., Hukins, D.W.L., Hunter, A., Korsunsky, A.M., Eds.; Newswood Limited: Hong Kong, 2007; Lecture Notes in Engineering and Computer Science; Volume II, pp. 1401–1406. Available online: <http://www.kirkup.info/papers/SKAT07.pdf> (accessed on 23 April 2023).
- Arenas, J.P. Numerical computation of the sound radiation from a planar baffled vibrating surface. *J. Comput. Acoust.* **2008**, *16*, 321–341. [CrossRef]
- Kirkup, S. The Boundary Element Method in Acoustics: A Survey. *Appl. Sci.* **2019**, *9*, 1642. [CrossRef]
- Tenenbaum, E.; Bucher, I. Reconstruction of a nonlinear acoustic field based on acousto-optic effect computational tomography. In Proceedings of the ISMA2022 including USD2022—International Conference on Noise and Vibration Engineering, Leuven, Belgium, 12–14 September 2022; KU Leuven: Leuven, Belgium, 2022; Paper ID 201 in Vol. Optical Methods; pp. 2750–2762. Available online: https://past.isma-isaac.be/downloads/isma2022/proceedings/Contribution_201_proceeding_3.pdf (accessed on 23 April 2023).
- Gardonio, P.; Guernieri, G.; Turco, E.; Rinaldo, R.; Fusiello, A. Reconstruction of the sound radiation field from plate flexural vibration measurements taken with multiple cameras. In Proceedings of the ISMA2022 including USD2022—International Conference on Noise and Vibration Engineering, Leuven, Belgium, 12–14 September 2022; KU Leuven: Leuven, Belgium, 2022; Paper ID 196 in Vol. Optical Methods; pp. 2826–2837. Available online: https://past.isma-isaac.be/downloads/isma2022/proceedings/Contribution_196_proceeding_3.pdf (accessed on 23 April 2023).
- Zanarini, A. On the estimation of frequency response functions, dynamic rotational degrees of freedom and strain maps from different full field optical techniques. In Proceedings of the ISMA2014 including USD2014—International Conference on Noise and Vibration Engineering, Leuven, Belgium, 15–17 September 2014; KU Leuven: Leuven, Belgium, 2014; pp. 1155–1169; In Vol. Dynamic Testing: Methods and Instrumentation, Paper ID 676. Available online: https://past.isma-isaac.be/downloads/isma2014/papers/isma2014_0676.pdf (accessed on 23 April 2023).
- Zanarini, A. Comparative studies on full field FRFs estimation from competing optical instruments. In Proceedings of the ICoEV2015 International Conference on Engineering Vibration, Ljubljana, Slovenia, 7–10 September 2015; University Ljubljana & IFToMM: Ljubljana, Slovenia, 2015; pp. 1559–1568; Paper ID 191. Available online: https://www.researchgate.net/publication/280013709_Comparative_studies_on_Full_Field_FRFs_estimation_from_competing_optical_instruments (accessed on 23 April 2023).

13. Zanarini, A. Broad frequency band full field measurements for advanced applications: Point-wise comparisons between optical technologies. *Mech. Syst. Signal Process.* **2018**, *98*, 968–999. [[CrossRef](#)]
14. Zanarini, A. Competing optical instruments for the estimation of Full Field FRFs. *Measurement* **2019**, *140*, 100–119. [[CrossRef](#)]
15. Van der Auweraer, H.; Steinbichler, H.; Haberstock, C.; Freymann, R.; Storer, D. Integration of pulsed-laser ESPI with spatial domain modal analysis: Results from the SALOME project. In Proceedings of the 4th International Conference on Vibration Measurements by Laser Techniques: Advances and Applications, Ancona, Italy, 21–23 June 2000; Volume 4072, pp. 313–322. [[CrossRef](#)]
16. Zanarini, A. On the exploitation of multiple 3D full-field pulsed ESPI measurements in damage location assessment. *Procedia Struct. Integr.* **2022**, *37*, 517–524. [[CrossRef](#)]
17. Zanarini, A. On the defect tolerance by fatigue spectral methods based on full-field dynamic testing. *Procedia Struct. Integr.* **2022**, *37*, 525–532. [[CrossRef](#)]
18. Zanarini, A. On the approximation of sound radiation by means of experiment-based optical full-field receptances. In Proceedings of the ISMA2022 including USD2022—International Conference on Noise and Vibration Engineering, Leuven, Belgium, 12–14 September 2022; KU Leuven: Leuven, Belgium, 2022; Paper ID 207 in Vol. Optical Methods; pp. 2735–2749. Available online: https://past.isma-isaac.be/downloads/isma2022/proceedings/Contribution_207_proceeding_3.pdf (accessed on 23 April 2023).
19. Zanarini, A. About the excitation dependency of risk tolerance mapping in dynamically loaded structures. In Proceedings of the ISMA2022 including USD2022—International Conference on Noise and Vibration Engineering, Leuven, Belgium, 12–14 September 2022; KU Leuven: Leuven, Belgium, 2022; Paper ID 208 in Vol. Structural Health Monitoring; pp. 3804–3818. Available online: https://past.isma-isaac.be/downloads/isma2022/proceedings/Contribution_208_proceeding_3.pdf (accessed on 23 April 2023).
20. Zanarini, A. Introducing the concept of defect tolerance by fatigue spectral methods based on full-field frequency response function testing and dynamic excitation signature. *Int. J. Fatigue* **2022**, *165*, 107184. [[CrossRef](#)]
21. Zanarini, A. Risk Tolerance Mapping in Dynamically Loaded Structures as Excitation Dependency by Means of Full-Field Receptances. In *Computer Vision & Laser Vibrometry*; Baqersad, J., Di Maio, D., Eds.; Chapter 9, Conference Proceedings of the Society for Experimental Mechanics Series; Springer Nature Switzerland AG: Cham, Switzerland, 2023; Volume 6, p. 14648. [[CrossRef](#)]
22. Zanarini, A. Experiment-based Optical Full-field receptances in the Approximation of Sound Radiation from a Vibrating Plate. In *Computer Vision & Laser Vibrometry*; Baqersad, J., Di Maio, D., Eds.; Chapter 4, Conference Proceedings of the Society for Experimental Mechanics Series; Springer Nature Switzerland AG: Cham, Switzerland, 2023; Volume 6, p. 14650. [[CrossRef](#)]
23. Zanarini, A. Dynamic behaviour characterization of a brake disc by means of electronic speckle pattern interferometry measurements. In Proceedings of the IDETC/CIE ASME International Design Engineering Technical Conferences & Computers and Information in Engineering Conference, Long Beach, CA, USA, 24–28 September 2005; pp. 273–280. [[CrossRef](#)]
24. Zanarini, A. Damage location assessment in a composite panel by means of electronic speckle pattern interferometry measurements. In Proceedings of the IDETC/CIE ASME International Design Engineering Technical Conferences & Computers and Information in Engineering Conference, Long Beach, CA, USA, 24–28 September 2005; pp. 1–8. [[CrossRef](#)]
25. Zanarini, A. Full field ESPI measurements on a plate: Challenging experimental modal analysis. In Proceedings of the XXV IMAC, Orlando, FL, USA, 19–22 February 2007; pp. 1–11. Paper s34p04. Available online: https://www.researchgate.net/publication/266896551_Full_field_ESPI_measurements_on_a_plate_Challenging_Experimental_Modal_Analysis (accessed on 23 April 2023).
26. Zanarini, A. Fatigue life assessment by means of full field ESPI vibration measurements. In Proceedings of the ISMA2008 Conference, Leuven Belgium, 15–17 September 2008; pp. 817–832. [[CrossRef](#)]
27. Zanarini, A. Full field ESPI vibration measurements to predict fatigue behaviour. In Proceedings of the IMECE2008 ASME International Mechanical Engineering Congress and Exposition, Boston, MA, USA, 31 October–6 November 2008; pp. 165–174. [[CrossRef](#)]
28. Zanarini, A. On the role of spatial resolution in advanced vibration measurements for operational modal analysis and model updating. In Proceedings of the ISMA2014 including USD2014—International Conference on Noise and Vibration Engineering, Leuven, Belgium, 15–17 September 2014; KU Leuven: Leuven, Belgium, 2014; pp. 3323–3336. Available online: https://past.isma-isaac.be/downloads/isma2014/papers/isma2014_0678.pdf (accessed on 23 April 2023).
29. Zanarini, A. Accurate FRFs estimation of derivative quantities from different full field measuring technologies. In Proceedings of the ICoEV2015 International Conference on Engineering Vibration, Ljubljana, Slovenia, 7–10 September 2015; University Ljubljana & IFToMM: Ljubljana, Slovenia, 2015; pp. 1569–1578. Paper ID 192. Available online: https://www.researchgate.net/publication/280013778_Accurate_FRF_estimation_of_derivative_quantities_from_different_full_field_measuring_technologies (accessed on 23 April 2023).
30. Zanarini, A. Full field experimental modelling in spectral approaches to fatigue predictions. In Proceedings of the ICoEV2015 International Conference on Engineering Vibration, Ljubljana, Slovenia, 7–10 September 2015; University Ljubljana & IFToMM: Ljubljana, Slovenia, 2015; pp. 1579–1588. Paper ID 193. Available online: https://www.researchgate.net/publication/280013788_Full_field_experimental_modelling_in_spectral_approaches_to_fatigue_predictions (accessed on 23 April 2023).

31. Zanmarini, A. Model updating from full field optical experimental datasets. In Proceedings of the ICoEV2015 International Conference on Engineering Vibration, Ljubljana, Slovenia, 7–10 September 2015; University Ljubljana & IFToMM: Ljubljana, Slovenia, 2015; pp. 773–782. Paper ID 193. Available online: https://www.researchgate.net/publication/280013876_Model_updating_from_full_field_optical_experimental_datasets (accessed on 23 April 2023).
32. Zanmarini, A. Full field optical measurements in experimental modal analysis and model updating. *J. Sound Vib.* **2019**, *442*, 817–842. [[CrossRef](#)]
33. Zanmarini, A. On the making of precise comparisons with optical full field technologies in NVH. In Proceedings of the ISMA2020 including USD2020—International Conference on Noise and Vibration Engineering, Leuven, Belgium, 7–9 September 2020; KU Leuven: Leuven, Belgium, 2020; pp. 2293–2308. Available online: https://past.isma-isaac.be/downloads/isma2020/proceedings/Contribution_695_proceeding_3.pdf (accessed on 23 April 2023).
34. Zanmarini, A. Chasing the high-resolution mapping of rotational and strain FRFs as receptance processing from different full-field optical measuring technologies. *Mech. Syst. Signal Process.* **2022**, *166*, 108428. [[CrossRef](#)]
35. Avitabile, P.; O’Callahan, J.; Chou, C.; Kalkunte, V. Expansion of rotational degrees of freedom for structural dynamic modification. In Proceedings of the 5th International Modal Analysis Conference, London, UK, April 6–9. 1987; pp. 950–955.
36. Heylen, W.; Lammens, S.; Sas, P. *Modal Analysis Theory and Testing*, 2nd ed.; Katholieke Universiteit Leuven: Leuven, Belgium, 1998; ISBN 90-73802-61-X.
37. Liu, W.; Ewins, D. The Importance Assessment of RDOF in FRF Coupling Analysis. In Proceedings of the IMAC 17th Conference, Kissimmee, FL, USA, 8–11 February 1999; pp. 1481–1487.
38. Research Network QUATTRO. *Final Report on RDOFs in QUATTRO Brite-Euram Project no: BE 97-4184*; Technical Report; European Commission Research Framework Programs; European Commission: Bruxelles, Belgium, 1998; p. 83.
39. Ewins, D.J. *Modal Testing—Theory, Practice and Application*, 2nd ed.; Research Studies Press Ltd.: Hertfordshire, UK, 2000; p. 400.
40. Friswell, M.; Mottershead, J.E. *Finite Element Model Updating in Structural Dynamics*; Solid Mechanics and Its Applications, Kluwer Academic Publishers; Springer: Cham, The Netherlands, 1995; p. 292. [[CrossRef](#)]
41. Haeussler, M.; Klaassen, S.; Rixen, D. Experimental twelve degree of freedom rubber isolator models for use in substructuring assemblies. *J. Sound Vib.* **2020**, *474*, 115253. [[CrossRef](#)]
42. Pogacar, M.; Ocepek, D.; Trainotti, F.; Cepon, G.; Boltezar, M. System equivalent model mixing: A modal domain formulation. *Mech. Syst. Signal Process.* **2022**, *177*, 109239. [[CrossRef](#)]
43. Kreis, T. *Handbook of Holographic Interferometry*; Wiley-VCH: Berlin, Germany, 2004. [[CrossRef](#)]
44. Rastogi, P.K. *Optical Measurement Techniques and Applications*; Artech House, Inc.: Nordwood, MA, USA, 1997.
45. Van der Auweraer, H.; Steinbichler, H.; Haberstock, C.; Freymann, R.; Storer, D.; Linet, V. Industrial applications of pulsed-laser ESPI vibration analysis. In Proceedings of the XIX IMAC, Kissimmee, Florida (FL), USA, 5–8 February 2001; pp. 490–496.
46. Craig, R.R. *Structural Dynamics: An Introduction to Computer Methods*; John Wiley & Sons Inc.: New York, NY, USA, 1981.
47. O’Callahan, J.; Avitabile, P.; Riemer, R. System Equivalent reduction Expansion Process (SEREP). In Proceedings of the VII International Modal Analysis Conference, Las Vegas, Nevada (NV), USA, 30 January–2 February 1989; Volume 1, pp. 29–37.
48. Williams, E.G. *Fourier Acoustics: Sound Radiation and Nearfield Acoustical Holography*; Elsevier Ltd.: Amsterdam, The Netherlands, 1999. [[CrossRef](#)]
49. Wind, J.; Wijnant, Y.; de Boer, A. Fast evaluation of the Rayleigh integral and applications to inverse acoustics. In Proceedings of the ICSV13, The Thirteenth International Congress on Sound and Vibration, Vienna, Austria, 2–6 July 2006; pp. 1–8.
50. Richards, E.L.; Song, H.C.; Hodgkiss, W.S. Acoustic scattering comparison of Kirchhoff approximation to Rayleigh-Fourier method for sinusoidal surface waves at low grazing angles. *J. Acoust. Soc. Am.* **2018**, *144*, 1269–1278. [[CrossRef](#)]
51. Conta, S.; Santoni, A.; Homb, A. Benchmarking the vibration velocity-based measurement methods to determine the radiated sound power from floor elements under impact excitation. *Appl. Acoust.* **2020**, *169*, 107457. [[CrossRef](#)]
52. Chelliah, K.; Raman, G.; Muehleisen, R.T. An experimental comparison of various methods of nearfield acoustic holography. *J. Sound Vib.* **2017**, *403*, 21–37. [[CrossRef](#)]
53. Bendat, J.S.; Piersol, A.G. *Random Data: Analysis and Measurement Procedures*, 3rd ed.; John Wiley & Sons Inc.: Hoboken, NJ, USA, 2000.
54. Wagner, P.; Huesmann, A.P.; van der Seijs, M.V. Application of dynamic substructuring in NVH design of electric drivetrains. In Proceedings of the ISMA2020 including USD2020—International Conference on Noise and Vibration Engineering, Leuven, Belgium, 7–9 September 2020; pp. 3365–3382. Available online: https://past.isma-isaac.be/downloads/isma2020/proceedings/Contribution_369_proceeding_3.pdf (accessed on 23 April 2023).
55. Mueller, T.; Haeussler, M.; Sedlmair, S.; Rixen, D.J. Airborne transfer path analysis for an e-compressor. In Proceedings of the ISMA2020 including USD2020—International Conference on Noise and Vibration Engineering, Leuven, Belgium, 7–9 September 2020; pp. 3351–3364. Available online: https://past.isma-isaac.be/downloads/isma2020/proceedings/Contribution_287_proceeding_3.pdf (accessed on 23 April 2023).
56. Allen, M.S.; Sracic, M.W. A new method for processing impact excited continuous-scan laser Doppler vibrometer measurements. *Mech. Syst. Signal Process.* **2010**, *24*, 721–735. [[CrossRef](#)]
57. Di Maio, D.; Ewins, D.J. Continuous Scan, a method for performing modal testing using meaningful measurement parameters; Part I. *Mech. Syst. Signal Process.* **2011**, *25*, 3027–3042. [[CrossRef](#)]

58. Baqersad, J.; Poozesh, P.; Niezrecki, C.; Avitabile, P. Photogrammetry and optical methods in structural dynamics—A review. In *Mechanical Systems and Signal Processing*; Elsevier: Amsterdam, The Netherlands, 2016. [CrossRef]
59. Del Sal, R.; Dal Bo, L.; Turco, E.; Fusiello, A.; Zanmarini, A.; Rinaldo, R.; Gardonio, P. Vibration measurements with multiple cameras. In Proceedings of the ISMA2020 including USD2020 - International Conference on Noise and Vibration Engineering, Leuven, Belgium, 7–9 September 2020; pp. 2275–2292. Available online: https://past.isma-isaac.be/downloads/isma2020/proceedings/Contribution_481_proceeding_3.pdf (accessed on 23 April 2023).
60. Del Sal, R.; Dal Bo, L.; Turco, E.; Fusiello, A.; Zanmarini, A.; Rinaldo, R.; Gardonio, P. Structural vibration measurement with multiple synchronous cameras. *Mech. Syst. Signal Process.* **2021**, *157*, 107742. [CrossRef]
61. Mas, P.; Sas, P. *Acoustic Source Identification Based on Microphone Array Processing*; Technical Report; Noise & Vibration Research Group, Mechanical Engineering Department, Katholieke Universiteit Leuven: Leuven, Belgium, 2004; In ISAAC 15, Course on Numerical and Applied Acoustics, Katholieke Universiteit Leuven, Belgium, Mechanical Engineering Department, Noise & Vibration Research Group. Available online: <https://www.isma-isaac.be> (accessed on 23 April 2023).
62. Allemang, R.J. The Modal Assurance Criterion—Twenty Years of Use and Abuse. *Sound Vib.* **2003**, *37*, 14–23.
63. Maynard, J.D.; Williams, E.G.; Lee, Y. Nearfield acoustic holography: I. Theory of generalized holography and the development of NAH. *J. Acoust. Soc. Am.* **1985**, *78*, 1395–1413. [CrossRef]
64. Veronesi, W.A.; Maynard, J.D. Nearfield acoustic holography (NAH) II. Holographic reconstruction algorithms and computer implementation. *J. Acoust. Soc. Am.* **1987**, *81*, 1307–1322. [CrossRef]
65. Press, W.H.; Teukolsky, S.A.; Vetterling, W.T.; Flannery, B.P. *Numerical Recipes in C: The Art of Scientific Computing*, 2nd ed.; Cambridge University Press: Cambridge, UK, 1992.

Disclaimer/Publisher’s Note: The statements, opinions and data contained in all publications are solely those of the individual author(s) and contributor(s) and not of MDPI and/or the editor(s). MDPI and/or the editor(s) disclaim responsibility for any injury to people or property resulting from any ideas, methods, instructions or products referred to in the content.